390285-3-T

Electromagnetic scattering and radiation from microstrip patch antennas and arrays residing in a cavity

J. M. Jin, J. L. Volakis, and A. Alexanian

Northrop Corporation
B2 Division
Pico Rivera CA 90660

April 1992

UMR0439

Electromagnetic Scattering and Radiation from Microstrip Patch Antennas and Arrays Residing in a Cavity

Abstract

A new hybrid method is presented for the analysis of the scattering and radiation by conformal antennas and arrays. The method employs a finite element formulation within the cavity and the boundary integral (exact boundary condition) for terminating the mesh. By virtue of the finite element discretization, the method has no restrictions on the geometry and composition of the cavity or its termination. Furthermore, because of the convolutional nature of the boundary integral and the inherent sparseness of the finite element matrix, the storage requirement is kept very low at $O(n)$. These unique features of the method have already been exploited in other scattering applications and have permitted the analysis of large size structures with remarkable efficiency. In this report, we describe the method's formulation and implementation for finite microstrip patch arrays with superstrate and substrate configurations. Also, various modelling approaches are investigated and implemented for characterizing a variety of feed structures to permit the computation of the input impedance and radiation pattern. Many computational examples are presented which demonstrate the method's versatility, modeling capability and accuracy.

Contents

1 Introduction

This project dealt with the development of a new method for computing the scattering and radiation by planar and conformal antennas such as those illustrated in Figures 1 and 2. It was motivated by the lack of available software for such characterizations which are in turn important for designing and analyzing telemetry antennas with minimal backscattering effects.

Our first objective with this project was to develop the proposed mathematical formulation for a configuration such as that shown in Figure 1 with as little geometrical and electrical restrictions as possible. This prompted use of the finite element method for modeling the cavity region (including feed and radiating elements). Also, to avoid compromise in accuracy, the mesh was terminated via the boundary integral equation which was enforced at the cavity aperture. A challenge was the concurrent solution of the systems which results from the finite element and boundary integral methods. This required the development of a suitable solution scheme that maintained an $O(n)$ memory demand. A unique iterative solution scheme making use of the biconjugate gradient method along with the fast fourier transform was therefore developed which proved very successful in accomplishing this goal.

Much of the effort during this phase of the project was expended in developing and coding the formulation with the aim of validating it as outlined in the proposal. However, because of the unusual success of the solution

method, we also proceeded with additional improvements of the formulation. In general, the method was demonstrated capable of characterizations dealing with finite size substrates, a variety of patch shapes, substrate/superstrates, lumped loads, various feeds, material homogeneities, distributed loads such as resistive sheets and parasitic elements of any shape and configuration. This is owed to the versatility and adaptability of the finite element method, making the method unique in this respect. It is thus suitable in forming the basis of a general purpose code for this most popular class of antennas. A distinct characteristic of the method over standard approaches is the elimination of the need to employ a green's function which involves the substrate/superstrate parameters and surrounding geometry. The derivation of such green's functions is not possible for most cases or must be redone for each individual geometry. In contrast, the proposed formulation makes use of the same free space green's function regardless of the antenna's geometrical properties. Variations in substrate geometry, antenna/feed shape and materials are treated in the context of the finite element method (FEM) whose formulation is unaffected by such variations.

Below we summarize the formulation of the proposed finite element boundary integral method (FE-BI) which was described at some detail in the first bimonthly report. This is followed by a section on the method's attributes and capabilities. Several computations of scattering and radia-

tion for various antennas configurations are also given which demonstrate the method's accuracy and versatility.

2 Formulation

Consider the three-dimensional structure illustrated in Figure 1. The specific configuration consists of a microstrip patch antennas or array residing on or embedded in the substrate. The whole structure is residing in a cavity which is recessed in a ground plane. We will denote the free space region above the plane ($z > 0$) as region I and that inside the cavity ($-t < z < 0$) as region II occupying the volume V. We will further assume that the cavity is filled with an inhomogeneous material having a relative permittivity $\epsilon_r(\mathbf{r})$ and relative permeability $\mu_r(\mathbf{r})$.

In accordance with the equivalence principle [6], the fields in the two regions can be decoupled by closing the aperture with a perfect conductor and introducing the equivalent magnetic current

$$\mathbf{M} = \mathbf{E} \times \hat{\mathbf{z}} \tag{1}$$

over the extent of the aperture, where $\mathbf{E}$ is the electric field at the aperture ($z = 0$). The field in region I is then due to the radiation caused by the equivalent current $\mathbf{M}$ residing on the ground plane and possibly by other impressed external sources $(\mathbf{J}_e, \mathbf{M}_e)$ in the upper half space. Accordingly, by

invoking image theory we have

$$\mathbf{H}^I(\mathbf{r}) = \mathbf{H}^i(\mathbf{r}) + \mathbf{H}^r(\mathbf{r}) - 2jk_0Y_0 \iint_S \bar{\bar{\mathrm{G}}}_0(\mathbf{r},\mathbf{r}') \bullet \mathbf{M}(\mathbf{r}')\, dS' \tag{2}$$

where $\mathbf{H}^i$ denotes the incident field due to $(\mathbf{J}_e, \mathbf{M}_e)$ and $\mathbf{H}^r$ is that reflected by the ground plane without the aperture. Also, $k_0 = 2\pi/\lambda$ is the free space wavenumber, $Z_0 = 1/Y_0$ is the free space intrinsic impedance, S denotes the planar surface area of the aperture and $\bar{\bar{\mathrm{G}}}_0$ is the free-space dyadic Green's function given by

$$\bar{\bar{\mathrm{G}}}_0(\mathbf{r},\mathbf{r}') = \left(\bar{\bar{\mathrm{I}}} + \frac{1}{k_0^2}\nabla\nabla\right) G_0(\mathbf{r},\mathbf{r}') \tag{3}$$

with

$$\bar{\bar{\mathrm{I}}} = \hat{\mathbf{x}}\hat{\mathbf{x}} + \hat{\mathbf{y}}\hat{\mathbf{y}} + \hat{\mathbf{z}}\hat{\mathbf{z}} \quad \text{and} \quad G_0(\mathbf{r},\mathbf{r}') = \frac{e^{-jk_0|\mathbf{r}-\mathbf{r}'|}}{4\pi|\mathbf{r}-\mathbf{r}'|}.$$

Note, however, that when the antenna is in the radiation mode, no external sources $(\mathbf{J}_e, \mathbf{M}_e)$ exist and, therefore, the first two terms on the right hand side of (2) disappear.

Enforcing continuity of the tangential electric fields across the aperture, we find that the field in region II can be represented by the radiation of the equivalent magnetic current $-\mathbf{M}$ and other impressed internal sources $(\mathbf{J}_i, \mathbf{M}_i)$ which can be used to model various feed structures. The fields in the two regions are then coupled by enforcing continuity of the tangential magnetic fields across the aperture. This gives

$$\hat{\mathbf{z}} \times \mathbf{H}^{\mathrm{I}}(\mathbf{M}, \mathbf{J}_e, \mathbf{M}_e) = \hat{\mathbf{z}} \times \mathbf{H}^{\mathrm{II}}(-\mathbf{M}, \mathbf{J}_i, \mathbf{M}_i) \quad \text{at} \quad z = 0 \tag{4}$$

where $\mathbf{H}^{\mathrm{I}}$ and $\mathbf{H}^{\mathrm{II}}$ denote the magnetic fields in regions I and II, respectively.

The fields in the cavity region (region II) can be formulated using the finite element method. Specifically, the cavity fields are demanded to satisfy the variational equation

$$\delta F = 0 \tag{5}$$

where the functional F is given by

$$\begin{aligned} F\left(\mathbf{E}^{\mathrm{II}}\right) &= \frac{1}{2}\iiint_V \left[\frac{1}{\mu_r}\left(\nabla\times\mathbf{E}^{\mathrm{II}}\right)\bullet\left(\nabla\times\mathbf{E}^{\mathrm{II}}\right) - k_0^2\epsilon_r\mathbf{E}^{\mathrm{II}}\bullet\mathbf{E}^{\mathrm{II}}\right] dV \\ &\quad + \iiint_V \left[jk_0Z_0\mathbf{J}_i\bullet\mathbf{E}^{\mathrm{II}} - \frac{1}{\mu_r}\mathbf{M}_i\bullet\left(\nabla\times\mathbf{E}^{\mathrm{II}}\right)\right] dV \\ &\quad + jk_0Z_0\oiint_{S_{\mathrm{cav}}}\left(\mathbf{E}^{\mathrm{II}}\times\mathbf{H}^{\mathrm{II}}\right)\bullet\hat{\mathbf{n}}\,dS \end{aligned} \tag{6}$$

if the variation is taken with respect to the electric field. In (6), V denotes the volume occupied by region II, S_{cav} corresponds to the surface that encloses V and $\hat{\mathbf{n}}$ denotes the unit vector normal to the surface, pointing away from the cavity. The second volume integral represents the radiation of the impressed internal sources $(\mathbf{J}_i, \mathbf{M}_i)$.

To solve (6), it is necessary that the fields be known over the surface specified by S_{cav}. Obviously, the boundary condition to be imposed on the conducting boundaries of the cavity and also on the surface of the patch antennas is

$$\hat{\mathbf{n}}\times\mathbf{E}^{\mathrm{II}} = 0 \tag{7}$$

Substituting this into (6) eliminates the portion of the surface integral over the conducting boundary of the cavity (that is, there is no power flow through the metallic portion of S_{cav}). It remains to specify the boundary condition over the cavity's aperture and this is given by (1). Enforcing the continuity condition (4), we obtain

$$\begin{aligned} F &= \frac{1}{2}\iiint_V \left[\frac{1}{\mu_r}\left(\nabla\times\mathbf{E}^{\text{II}}\right)\bullet\left(\nabla\times\mathbf{E}^{\text{II}}\right) - k_0^2\epsilon_r\mathbf{E}^{\text{II}}\bullet\mathbf{E}^{\text{II}}\right] dV \\ &\quad + \iiint_V \left[jk_0Z_0\mathbf{J}_i\bullet\mathbf{E}^{\text{II}} - \frac{1}{\mu_r}\mathbf{M}_i\bullet\left(\nabla\times\mathbf{E}^{\text{II}}\right)\right] dV \\ &\quad - 2k_0^2\iint_S \mathbf{M}(\mathbf{r})\bullet\left[\iint_S \bar{\bar{\mathrm{G}}}_0(\mathbf{r},\mathbf{r}')\bullet\mathbf{M}(\mathbf{r}')\,dS'\right] dS \\ &\quad - jk_0Z_0\iint_S \mathbf{M}(\mathbf{r})\bullet\left[\mathbf{H}^i(\mathbf{r})+\mathbf{H}^r(\mathbf{r})\right] dS \end{aligned} \tag{8}$$

which can be discretized via the finite element method for a solution of $\mathbf{M}$ and the internal field $\mathbf{E}^{\text{II}}$. Once $\mathbf{M}$ is found, the far zone scattered or radiated field can be easily computed from

$$\mathbf{H}^s(\mathbf{r}) = -jk_0Y_0\frac{e^{-jk_0r}}{2\pi r}\iint_S(\hat{\theta}\hat{\theta}+\hat{\phi}\hat{\phi})\bullet\mathbf{M}(x',y')e^{jk_0\sin\theta(x'\cos\phi+y'\sin\phi)}\,dx'\,dy' \tag{9}$$

where (r,θ,ϕ) are the usual spherical coordinates of the observation point. The radar cross section (RCS) of the structure is then given by

$$\sigma = \lim_{r\to\infty} 4\pi r^2\frac{|\mathbf{H}^s(\mathbf{r})|^2}{|\mathbf{H}^i(\mathbf{r})|^2}. \tag{10}$$

The input impedance and antenna gain can also obtained from the solution of $\mathbf{E}^{\text{II}}$.

The discretization of the functional F as given in (8) was accomplished by subdividing the cavity volume as a collection of rectangular bricks (not necessarily of equal sides). Within each brick the fields were then expanded in terms of edge-based or vector basis functions. The coefficients of this expansion correspond to the fields parallel to each edge forming the rectangular brick. In contrast to the usual nodal basis/shape functions the aforementioned vector bases are rid of several shortcomings. Most importantly, they are not associated with spurious resonances and are further well behaved at metallic corners and edges. As a result, the resulting system is well-behaved and converges more rapidly than usual.

The details of the discretization of F are given in the first bimonthly report and are thus omitted here. In general, the resulting system can be written in the form

$$[A]\{\phi\} = \{b\} \tag{11}$$

where $[A]$ is a symmetric matrix composed of a large sparse submatrix and a small full submatrix which is associated with the aperture nodes. The column $\{\phi\}$ represents the unknown element edge fields and $\{b\}$ is the resultant excitation vector. A most efficient method for solving this system is the biconjugate gradient (BicG) method. The required solution algorithm is as follows:

Initialize the residual and search vectors with an initial guess x_0:

$$p_0 = r_0 = b - Ax_0$$

Iterate for $k = 0, 1, 2, \ldots$:

$$\begin{aligned} \alpha_k &= \frac{\langle r_k, r_k \rangle}{\langle p_k, Ap_k \rangle} \\ x_{k+1} &= x_k + \alpha_k p_k \\ r_{k+1} &= r_k - \alpha_k Ap_k \\ \beta_k &= \frac{\langle r_{k+1}, r_{k+1} \rangle}{\langle r_k, r_k \rangle} \\ p_{k+1} &= r_{k+1} + \beta_k p_k \end{aligned}$$

Terminate when

$$\text{err} = \frac{\|r_{k+1}\|}{\|b\|} < \text{tolerance.}$$

In the algorithm, $\langle x, y \rangle = x^T y$, where T denotes the transpose of the column.

The memory required for implementing this solution algorithm is approximately

$$120N_t + 100N_b$$

where

N_t = total numbers of unknowns

N_b = number of unknowns at the aperture.

Clearly, this is a relatively low memory demand for an exact solution, and an important attribute of the method.

In the next section we present various applications of the formuulation which demonstrate its versatility, efficiency, accuracy and overall capability. However, before doing so we first discuss the modeling of various configurations which will be encountered in these applications.

3 Modeling considerations

In this section we consider the modelling of the conducting patches, microstrip transmission lines, impedance loads, resistive cards, shorting pins and coaxial feeds in the context of the finite element – boundary integral formulation. We also discuss some computational aspects related to the implementation of the technique.

3.1 Conducting patches and microstrip transmission lines

The modelling of the conducting patches is straightforward and is carried out by setting the tangential electric field components to zero for the element sides coinciding with the patch. The modelling of microstrip transmission lines is treated in exactly the same manner. We remark, though, that owing to the use of the edge-based expansion functions, no special condition needs to be imposed on the transverse components of the electric field at the patch

or stripline edges.

3.2 Impedance loads and shorting pins

An impedance load of Z_L ohms can be modelled as a post of finite conductivity joining both the patch and the base of the cavity. Assuming a post of length l and cross section s, the required conductivity of the post to represent the load must be $\sigma = l/(Z_L s)$. Accordingly, its contribution to the matrix element A_{ij} is

$$\frac{jk_0 Z_0 l}{Z_L s} \iiint_v \mathbf{N}_i^e \bullet \mathbf{N}_j^e \, dv$$

where the integration is over the volume of the post and $\mathbf{N}_j^e$ are the shape functions. Provided the post is very thin, this reduces to $jk_0 Z_0 l^2 \mathbf{N}_i^e \bullet \mathbf{N}_j^e / Z_L$, where $\mathbf{N}_i^e \bullet \mathbf{N}_j^e$ takes its value at the position of the post. Further, if the thin post is coincident with the ith edge, then it only contributes to A_{ii} and this contribution is $jk_0 Z_0 l^2 / Z_L$. The short-circuit ($Z_L = 0$) condition is usually realized with a shorting pin and two approaches can be used in this case. One approach is to represent it with a post of high conductivity and another is to simply set the electric field along the post to zero. We have observed that the final solution is unaffected by the choice of the model.

3.3 Coaxial feeds and gap generators

We consider two types of models for simulating a coaxial feed via this technique. For thin substrates the coaxial feed may be replaced by a current

filament and in this case, the contribution to the matrix element is simply $jk_0Z_0l\mathbf{I} \bullet \mathbf{N}_i^e$, where $\mathbf{I}$ denotes the electric current of the filament and l is its length. For thicker substrates a magnetic frill current model may be employed. In this case, the inner conductor of the coaxial feed is modelled as a conducting post and an equivalent magnetic current is introduced over the aperture of the coaxial feed. This is similar to the treatment for the cavity aperture, except that the free space region is now replaced by the coaxial waveguide. Finally, one may resort to a simple gap generator for the excitation whose modelling amounts to specifying *a priori* the field across the gap.

3.4 Resistive cards

A resistive sheet is an infinitesimally thin sheet of certain resistivity R (Ω per square), capable of supporting an electric current flowing on its surfaces. In practice, these sheets are made by sputtering/spraying conducting material on a thin membrane whose dielectric constant is nearly unity. Mathematically, the sheet can be modelled by enforcing the boundary condition

$$\hat{\mathbf{n}} \times (\hat{\mathbf{n}} \times \mathbf{E}) = -R\,\mathbf{J}_s \tag{12}$$

where $\hat{\mathbf{n}}$ denotes the outward unit vector normal to the resistive sheet, $\mathbf{J}$ denotes the current on the sheet and $\mathbf{E}$ is the field measured at the location of the sheet. Whereas the tangential electric field is continuous across the

resistive sheet, the introduction of the surface current creates a discontinuous tangential magnetic field. Assuming that the magnetic field on one side is $\mathbf{H}^+$ (A/m) and that on the other side is $\mathbf{H}^-$ (A/m) ($\hat{\mathbf{n}}$ points from the "–" side to "+" side), from (36) we have

$$\hat{\mathbf{n}} \times (\hat{\mathbf{n}} \times \mathbf{E}) = -R\, \hat{\mathbf{n}} \times (\mathbf{H}^+ - \mathbf{H}^-). \tag{13}$$

Because of the discontinuous magnetic field, the functional F given by (6) or (8) must be supplemented with the addition of a boundary integral over the surface of the resistive card S_r. Essentially, this implies that the last surface integral must now be carried out over S_{cav} and over both sides of the resistive surface S_r. For continuous magnetic fields at S_r the sum of the integrals from each side of the surface S_r would, of course, yield zero contribution. This is not, however, the case when the condition (36) is imposed at S_r, in which case the functional (6) must be supplemented by the terms

$$jk_0 Z_0 \iint_{S_r} \mathbf{E} \bullet (\mathbf{H}^- \times \hat{\mathbf{n}})\, dS \tag{14}$$

and

$$-jk_0 Z_0 \iint_{S_r} \mathbf{E} \bullet (\mathbf{H}^+ \times \hat{\mathbf{n}})\, dS. \tag{15}$$

Combining the two integrals and invoking the resistive sheet condition (2) we obtain

$$-jk_0 Z_0 \iint_{S_r} \frac{1}{R} \mathbf{E} \bullet [\hat{\mathbf{n}} \times (\hat{\mathbf{n}} \times \mathbf{E})]\, dS$$

$$= jk_0 Z_0 \iint_{S_r} \frac{1}{R}(\hat{\mathbf{n}} \times \mathbf{E}) \bullet (\hat{\mathbf{n}} \times \mathbf{E})\, dS \qquad (16)$$

and as noted before, R denotes the resistivity of the resistive sheet and it was not factored out of the integral since it can be a function of position. As a result, (6) can be written as

$$\begin{aligned} F(\mathbf{E}) \;=\; & \frac{1}{2}\iiint_V \left[\frac{1}{\mu_r}(\nabla \times \mathbf{E}) \bullet (\nabla \times \mathbf{E}) - k_0^2 \epsilon_r \mathbf{E} \bullet \mathbf{E}\right] dV \\ & + \iiint_V \left[jk_0 Z_0 \mathbf{J}_i \bullet \mathbf{E} - \frac{1}{\mu_r}\mathbf{M}_i \bullet (\nabla \times \mathbf{E})\right] dV \\ & + jk_0 Z_0 \oiint_{S_{\text{cav}}} (\mathbf{E} \times \mathbf{H}) \bullet \hat{\mathbf{n}}\, dS \\ & + jk_0 Z_0 \iint_{S_r} \frac{1}{R}(\hat{\mathbf{n}} \times \mathbf{E}) \bullet (\hat{\mathbf{n}} \times \mathbf{E})\, dS \qquad (17) \end{aligned}$$

The integral over S_r is discretized following the procedure outlined above, i.e. by replacing the fields with their expansion given in (16).

4 Applications

To demonstrate the method's versatility, capability and accuracy, a computer code was written on the basis of the proposed formulation. This code employs its own mesh generator and was used to compute the scattering the radiation for a variety of antenna configurations. Several of these computations were already reported in the second bimonthly report. Here we summarize these results and we incorporate a few more. In addition, we also show some results scattering by a finite array of metal cavities. These results relate to a

companion project but are included here because they are based on the same formulation.

Test Example 1: RCS of a single patch residing in a finite cavity

The geometry of this configuration is given in Figure 3. The patch is 1.448in $\times$ 1.038in and resides on a dielectric substrate having thickness $t = 0.057$in and relative permittivity $\epsilon_r \approx 4.0$. The substrate is housed in a 2.89in $\times$ 2.10in $\times$ 0.057in rectangular cavity recessed in a ground plane. This configuration is subjected to a $\hat{\theta}$ polarized plane wave incident in the xz plane. The backscatter xz pattern for this excitation at 9.2GHz is shown in Figure 4 and is seen to be in good agreement with the measured data [1]. Figure 5 shows the corresponding backscatter pattern of the cavity in isolation (i.e. patch is removed). As seen, the calculated pattern is again in good agreement with the measured data.

Test Example 2: Input impedance computation with probe feed

The specific antenna geometry is shown in Figure 6 consisting of a patch 3.4cm $\times$ 5.0cm residing at the aperture of a 7.5cm $\times$ 5.1cm cavity. The substrate is of thickness $t = 0.08779$ and has a relative permittivity $\epsilon_r = 2.17$ with a loss tangent of 0.0015. Figure 7 shows the complex input impedance as a function of frequency with the probe feed placed at (1.22cm, 0.85cm).

These calculations were done in the presence of a 50Ω resistor (lumped load) placed between the patch and substrate at (−2.2cm, −1.5cm). Our calculations are seen to be in good agreement with the measured data [2] whereas corresponding calculations using traditional methods are not as accurate. We remark that the 50Ω load (50Ω resistive) serves to reduce the RCS of the patch at resonance. However, it also reduces the antenna gain. It has been observed though that at resonance the dB reduction in RCS is twice that of the gain (i.e. if the gain is reduced by 5dB, the RCS will be reduced by approximately 10dB). Unfortunately, the resistors do not have any appreciable effect on the RCS when the patch is illuminated with a frequency out of its resonant frequency.

Test Example 3: Input impedance of a microstrip line feed patch

The specific configuration is illustrated in Figure 8. It is a 4.02cm × 4.02cm patch fed by a 50Ω microstrip line at 2.01cm from the nearest corner. The substrate is 0.159cm thick and has a permittivity of $\epsilon_r = 2.55$ with a loss tangent of $\tan\delta = 0.002$. Figure 9 shows on a Smith chart the calculated input impedance referenced to the point where the microstrip line joins the patch. The different points comprising the contour on the chart correspond to different calculation frequencies. Except for a slight shift in frequency, it is seen that our calculations are in good agreement with those given by

Bailey and Deshpande [3], who employed the traditional moment method. It should be remarked though that for our calculations the patch was placed on a finite substrate whereas those in [3] were computed for an infinite one. The agreement shown in Figure 9 simply points out that the finite substrate does not play a significant role on the radiation properties of the patch.

Test example 4: Input impedance of a strip line fed microstrip patch

The configuration is illustrated in Figure 10. The patch is 2.5cm $\times$ 4.0cm and resides on a finite substrate of size 7.5cm $\times$ 7.5cm. The stripline is 0.5cm wide and is sandwiched between two dielectric layers each of thickness 0.15cm and having $\epsilon_r = 2.2$. It is electromagnetically coupled to the patch as illustrated in the figure. The input impedance (referred to A) for this configuration is plotted on a Smith chart in Figure 11 for different frequencies about resonance. The S_{11} parameter for a similar configuration is plotted in Figure 10.

Test example 5: Radiation pattern of a single patch

The geometry of the pertinent patch is given in Figure 12 along with the associated E and H-plane radiation pattern at $f = 2.62$GHz. The patch is 3.66cm $\times$ 3.66cm and resides at the aperture of a 5.20cm $\times$ 7.32cm the substrate is of thickness 0.158cm, has permittivity $\epsilon_r = 2.17$ and a loss tangent

$\tan\delta = 0.001$. We remark that cavity terminations have negligible effect on the radiation pattern and the same is true for the feed point. However, the input impedance is strongly dependent on the location and type of the feed.

Test example 6: Radiation pattern of a 3×3 patch array

The patches of this array are identical to those described in test example 5. They are 5.49cm apart in the x-direction and 3.90cm apart in the y-direction and reside in the aperture of a 18.3cm $\times$ 13.0cm. With the patches uniformly fed, the E and H radiation patterns are shown in Figure 14 and these were computed at 2.92GHz.

Test example 7: Radiation pattern of a 200 element array

This is a 13×16 element array. Each element is identical to that in test example 5 and is separated from its adjacent the same distances given in test example 6. The radiation pattern of this array is of the expected form and is shown in Figure 15. What is impressive though is the size of the system (more than 120,000 unknowns) which was solved to generate this pattern. Most impressive is the fast convergence of the solution. Normally most iterative routines converge in $N/3$ iterations whereas this system converged in only 100 iterations!

Test example 8: Characterization of a dielectrically coated patch

To reduce the RCS of the patch we consider the possibility of coating it with a lossy ferrite material as shown in Figure 16. The RCS of this patch as a function of the coating's thickness is shown in Figure 17. It is clearly seen that the RCS is reduced more than the gain, which is a desirable result. We remark that the calculations in Figure 17 were performed at the resonant frequency of the coated patch which is plotted in Figure 18. The input impedance of the coated patch at the resonant frequency is shown in Figure 19. Finally, a plot of the RCS as a function of frequency for the coated patch with $t = 0.15$cm is given in Figure 20. The RCS peaks occur at the resonant frequency. It is observed that although the coating reduces the RCS in the operating band of the patch it does not do the same away from resonance.

Test example 9: Characterization of a patch loaded with a resistive skirt

As seen from test example 8, the placement of a dielectric coating did not reduce the RCS of the patch. In fact, the RCS was increased for frequencies above resonance. The usual approach for reducing the RCS at resonance is to place lumped loads (see test example 2) at the patch edges and this reduces the RCS and gain (dB RCS reduction is twice that of the gain) of the patch. However, it was found that the lumped loads do not affect the RCS above resonance where the structural contribution of the patch plays

a significant role. After some investigation, we found that a rather effective method for reducing the RCS at higher frequencies without substantially affecting the patch's radiation performance performance was to attach a thin ribbon of resistive sheet at the patch's edges as shown in Figure 21. The corresponding RCS of the patch with and without the resistive skirt is shown in the same figure, and it is seen that the R-skirt nearly eliminates all resonant characteristics of the patch above the first resonance. In contrast the gain of the patch at the first resonance is only nominally reduced by 4–5 dB, as illustrated in Figure 22. The radiation pattern is unaffected.

Test example 10: Scattering by a 5×5 cavity array

This example demonstrates the method's capability in modeling radomes and arrays of patches residing in different but adjacent cavities. Such is the nature of the configuration depicted in Figure 23, which displays an array of 5×5 patches residing in individual rectangular metallic cavities. For our computations the cavity base will be assumed metallic, but if kept open, the array may then represent a bandpass radome. The radiating element can be placed anywhere in the cavity, but its most usual position is at the aperture, as shown. The reflection coefficient and active resistance of such an array as a function of scanning angle is shown in Figure 24. For this particular example, there is obviously no blindness angle other than at grazing. How-

ever, blindness may occur at other angles as well, even when the cavities are separated by metallic walls. Thus, the lack or presence of surface waves does not necessarily control the blindness angles of the array.

The backscatter RCS patterns for a similar 5×5 cavity array with the patch removed is shown in Figure 25. These patterns are compared with measured data and the agreement is indeed excellent. Two grating lobes are seen in these patterns. One occurs at 23 degrees from normal and the other is seen at about 55 degrees.

5 Conclusions

From the above, it is quite clear that we have developed a new formulation which is rid of the usual limitations associated with previous numerical approaches. Such approaches are suited for special purpose antennas, i.e. either rectangular or circular patches but not both; do not allow for lumped and distributed loading and are only suited for simple feed models; do not readily permit variations in antenna shape and conformity; do not permit modeling of finite length substrates/superstrates; are not suited for finite size arrays and do not account for coupling effects associated with substrate terminations. Moreover, the analysis of circularly conformal arrays has been beyond their reach in spite of continuous attempts to develop a usable analysis based on traditional methods. The developed method does not suffer

from these geometrical/modeling limitations and is computationally efficient. It is therefore well suited in forming the basis of the software platform for the analysis and design of conformal microstrip patch antennas and arrays. The development of such a platform requires the incorporation of several peripheral software for defining the geometry, the finite element mesh, the desired output parameters and an appropriate user interface. As outlined in our subsequent proposal, the analytical methodology must also be modified to allow for cylindrically curved antennas and arrays, since the present development was intentionally restricted to planar arrays. The methodology is still applicable to this type of antenna configuration but must be revised to employ a different green's function and volume element for discretizing the cylindrical substrate/superstrate.

References

[1] J.-M. Jin and J. L. Volakis, "A hybrid finite element method for scattering and radiation by microstrip patch antennas and arrays residing in a cavity," *IEEE Trans. Antennas Propagat.*, vol. AP–39, pp. 1598–1604, Nov. 1991.

[2] D. P. Forrai and E. H. Newman, "Radiation and scattering from loaded microstrip antennas over a wide bandwidth," Ohio State Univ., Columbus, Tech. Rep. 719493–1, Sept. 1988.

[3] M. D. Deshpande and M. C. Bailey, "Input impedance of microstrip antennas," *IEEE Trans. Antennas Propagat.*, vol. AP–30, pp. 645–650, July 1982.

List of Figures

Figure 12. Calculated S_{11} scattering coefficient to the stripline-fed patch shown in Figure 10.

Figure 13. Calculated E and H plane radiatio pattern of the illustrated cavity-backed patch at 2.62GHz. The feed is at (1.31cm, 0.78cm), the patch size is 3.66cm $\times$ 2.60cm. The substrate is housed in a 7.32cm $\times$ 5.20cm $\times$ 0.158cm cavity.

Figure 14. Calculated E and H plane radiation patterns of a 3×3 cavity-backed patch array at 2.62GHz. The patches are uniformly fed and identical in size to that in Figure 13. Their centers are 5.49cm apart in the x-direction and 3.90cm apart in the y-direction. The entire array is housed in 18.3cm $\times$ 13cm $\times$ 0.158cm cavity.

Figure 15. Calculated E and H plane radiation pattern of the illustrated 13×16 element array at 2.62GHz. Each patch is identical to that shown in Figure 13 and their separation is the same as that associated with array in Figure 14.

Figure 16. Geometry of the dielectrically coated patch. The coating has $\epsilon_r = 10.2 - j3.8$, $\mu_r = 2.12 - j1.5$. The lower substrate has $\epsilon_r = 2.17$.

Figure 17. Normal incidence normalized RCS and Gain of the patch in Figure 15 as a function of coating thickness at the resonant frequency.

Figure 18. Resonant frequency of the coated patch in Figure 16 as a function of coating thickness.

Figure 19. Input resistance of the coated patch in Figure 16 as a function of coating thickness.

Figure 20. Normal incidence RCS of the coated patch in Figure 16 as a function of frequency. Comparison of data calculated with and without a coating of thickness 0.15cm.

Figure 21. Geometry of the patch loaded with a resistive skirt at the edges and its backscatter RCS as a function of frequency. The RCS was computed at an incidence angle of 70 degrees from the normal.

Figure 22. Gain and RCS of the patch in Figure 21 at near resonance.

Figure 23. Array of patches residing on the surface of individual rectangular cavities.

Figure 24. Reflection coefficient and active resistance as a function of scan angle for the 5×5 cavity-backed patch array in Figure 23. For this computation $T_x = T_y = 5$cm, the cavity size is 4.5cm $\times$ 4.5cm $\times$ 0.2cm, $f = 3$GHz and the patch size is 3cm $\times$ 3cm. Also, the cavity is filled with a dielectric having $\epsilon_r = 2.80$.

Figure 25. Principal backscatter pattern of the 5×5 cavity array shown in Figure 23 with the patch removed. For this computation $T_x = T_y = 4$cm, $d = 0.45$cm, and $f = 9.1$GHz. (a) E_θ pattern; (b) E_ϕ pattern.

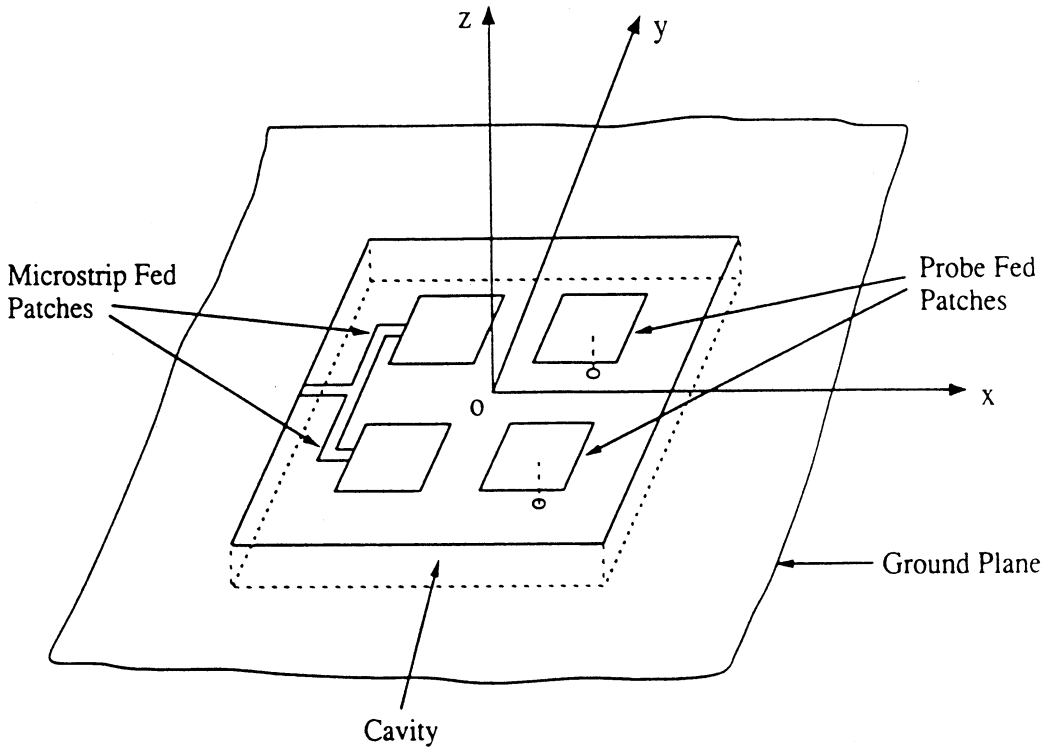

Fig. 1 Geometry of a microstrip patch array in a cavity.

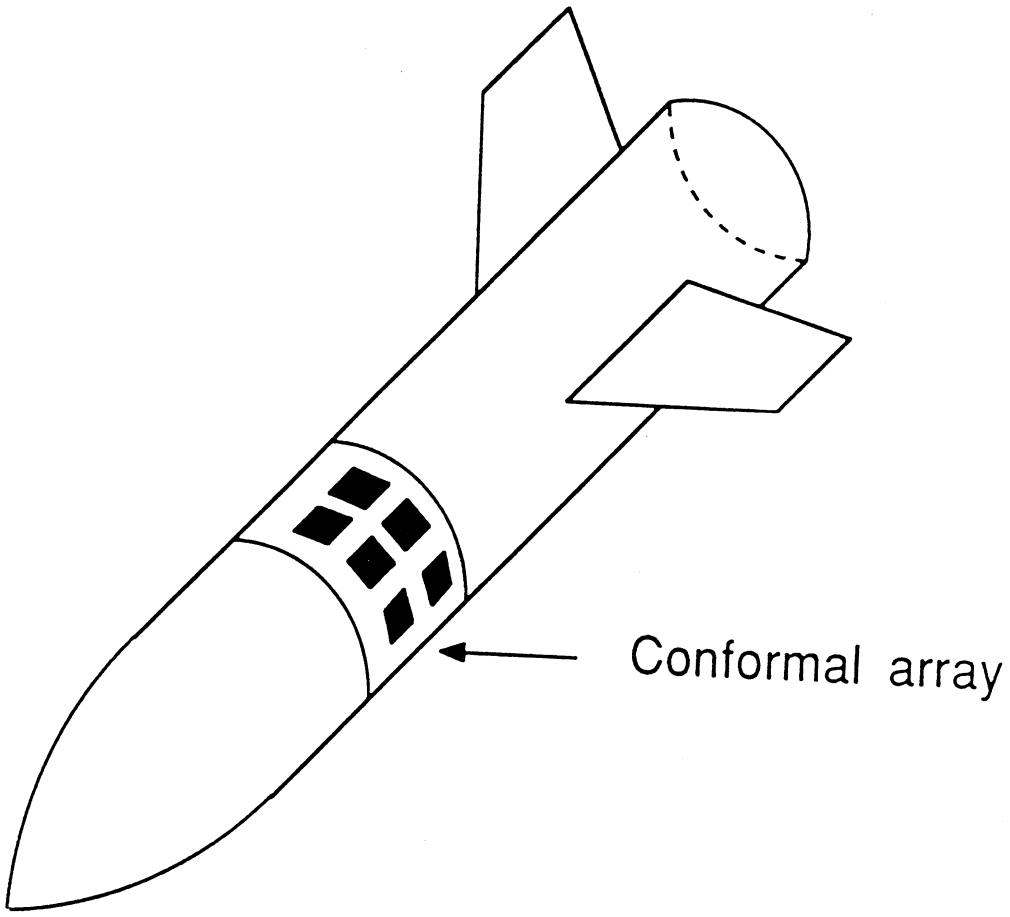

Figure 2. Geometry of a conformal microstrip patch array.

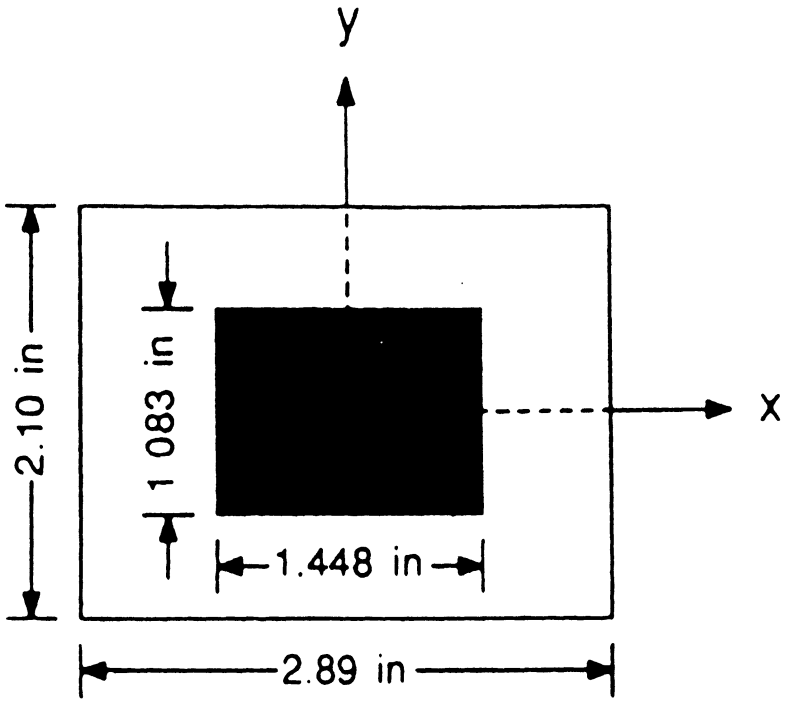

Figure 3. Geometry of the cavity-backed patch antenna whose radar cross section is given in Figures 4 and 5. The cavity's depth is 0.057 inches and the substrate has $\epsilon_r = 4$.

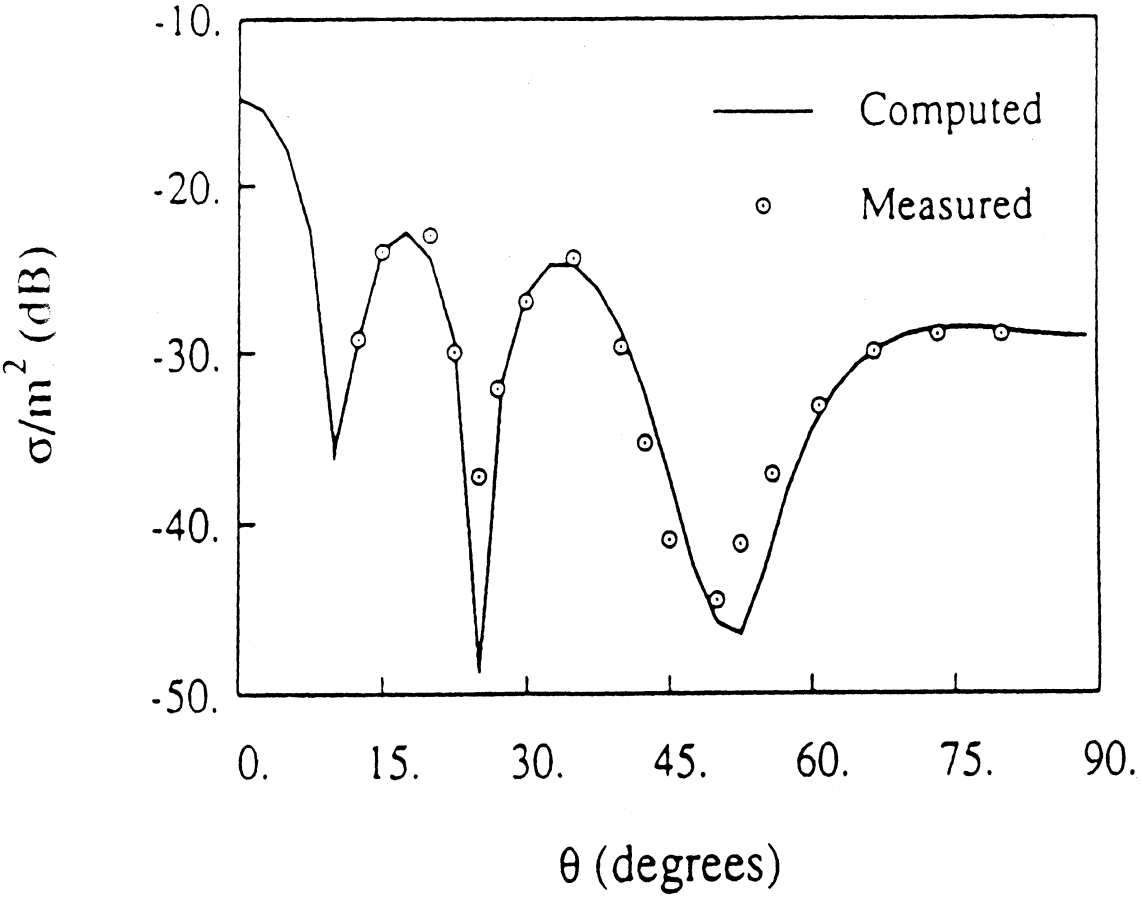

Figure 4. Comparison of the computed and measured θ-polarized xz-plane backscatter RCS of the planar antenna shown in Figure 3 at 9.2 GHz.

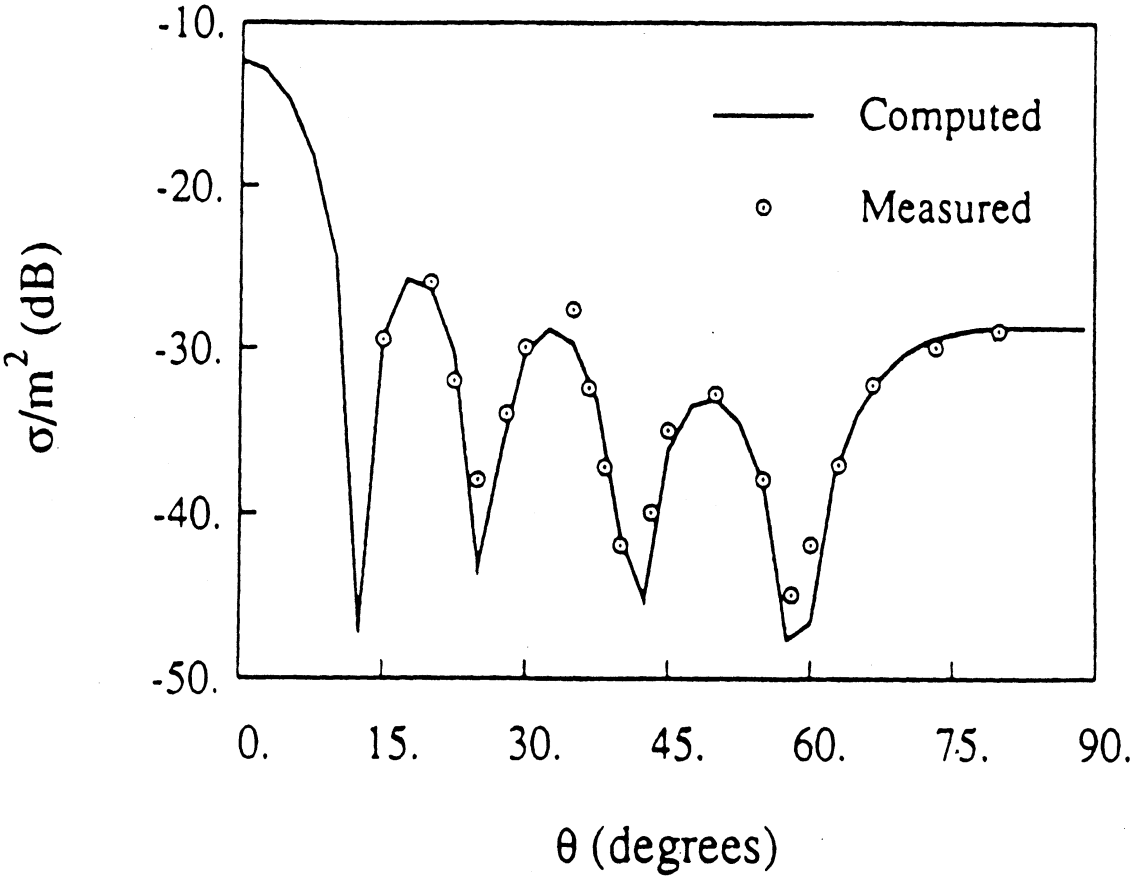

Figure 5. Computed and measured θ-polarized xz-plane backscatter RCS of the cavity shown in Figure 3 with the patch removed at 9.2GHz.

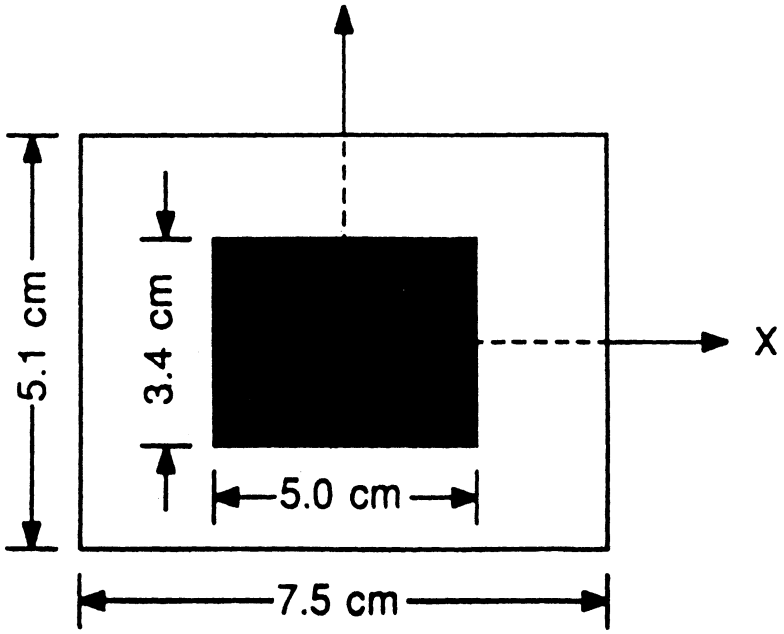

Figure 6. Geometry of the cavity-backed probe-fed patch antenna whose input impedance is given in Figure 7. The cavity's depth is 0.08779cm and has $\epsilon_r = 2.17$ with a loss tangent of 0.0015.

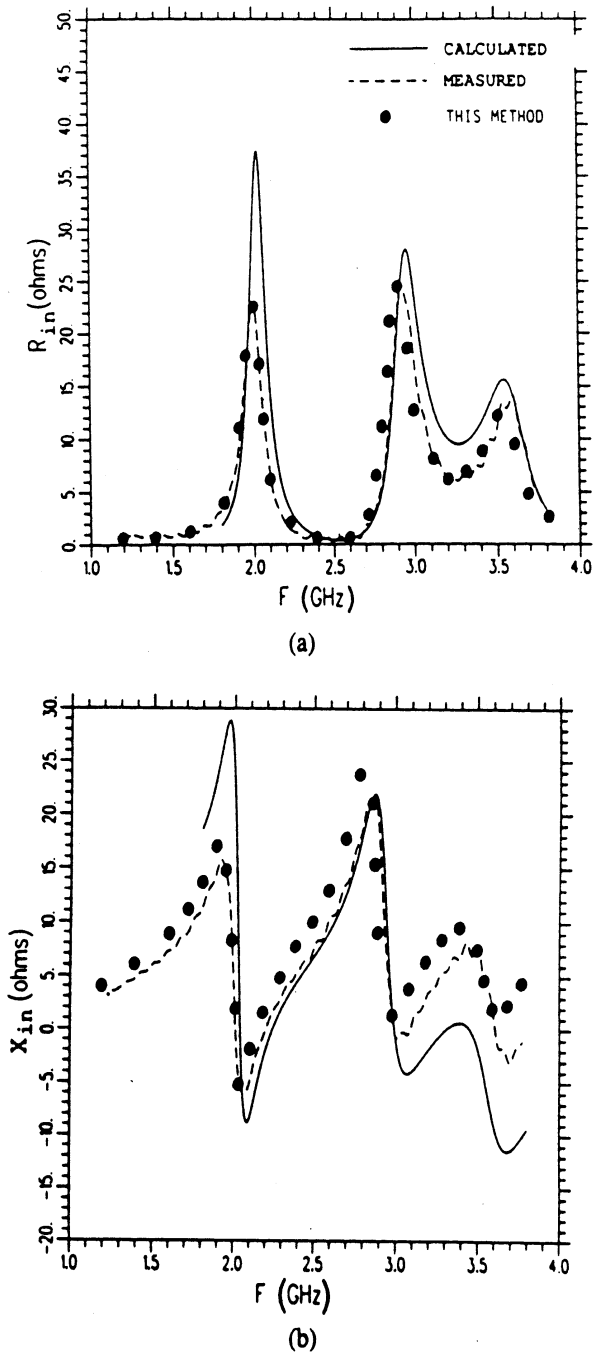

Figure 7. Comparison of computed and measured [2] input impedances of the probe-fed patch shown in Figure 6 loaded with a 50Ω resistor at (x_L = −2.2cm, y_L = −1.5cm). The probe feed is at (x_f = 1.22 cm, y_f = 0.85cm). (a) Real part; (b) reactive part.

x measured [3]

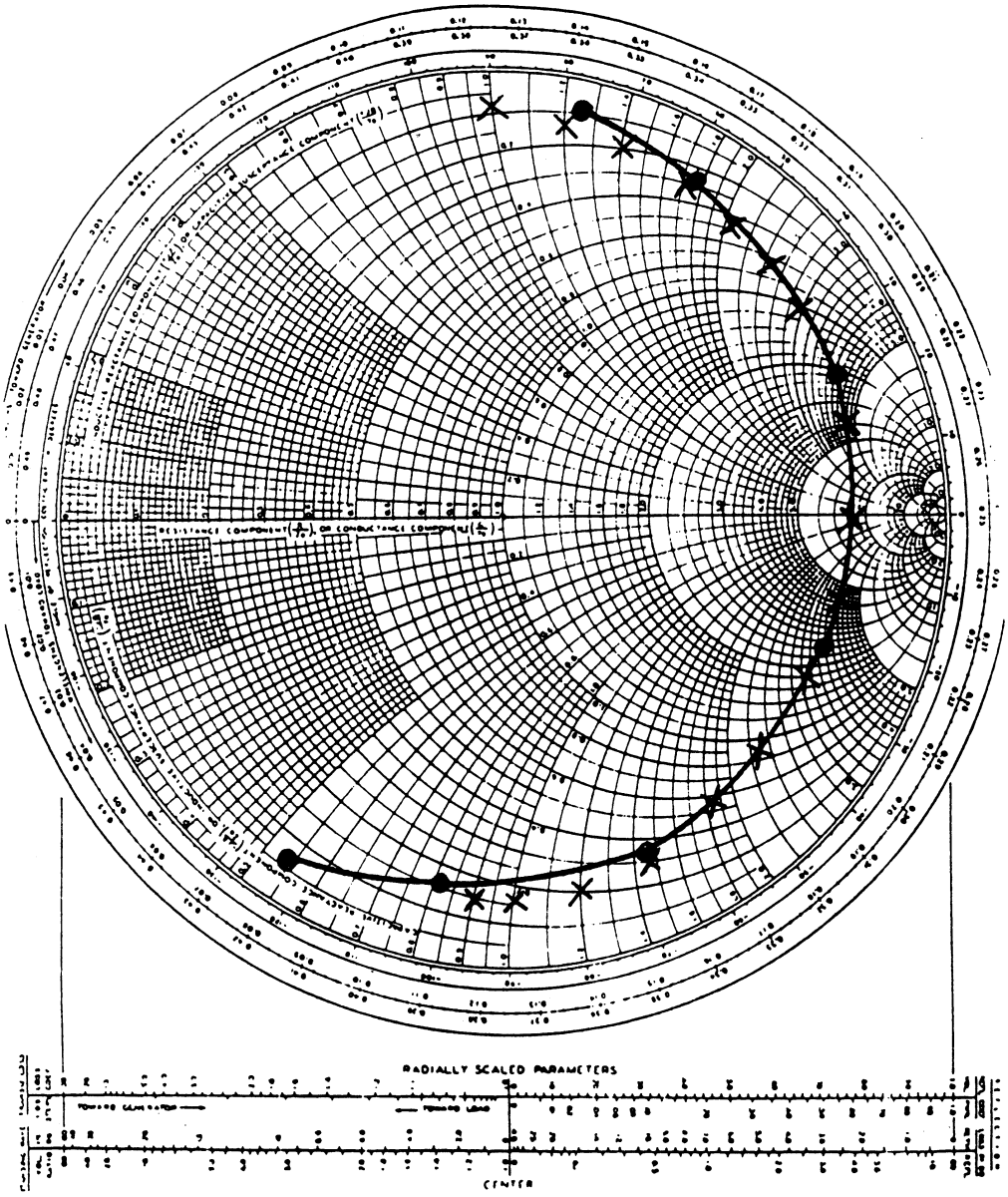

Figure 9. Comparison of the computed and measured input impedance (referenced to the junction between the patch and microstrip line) for the patch antenna shown in Figure 8.

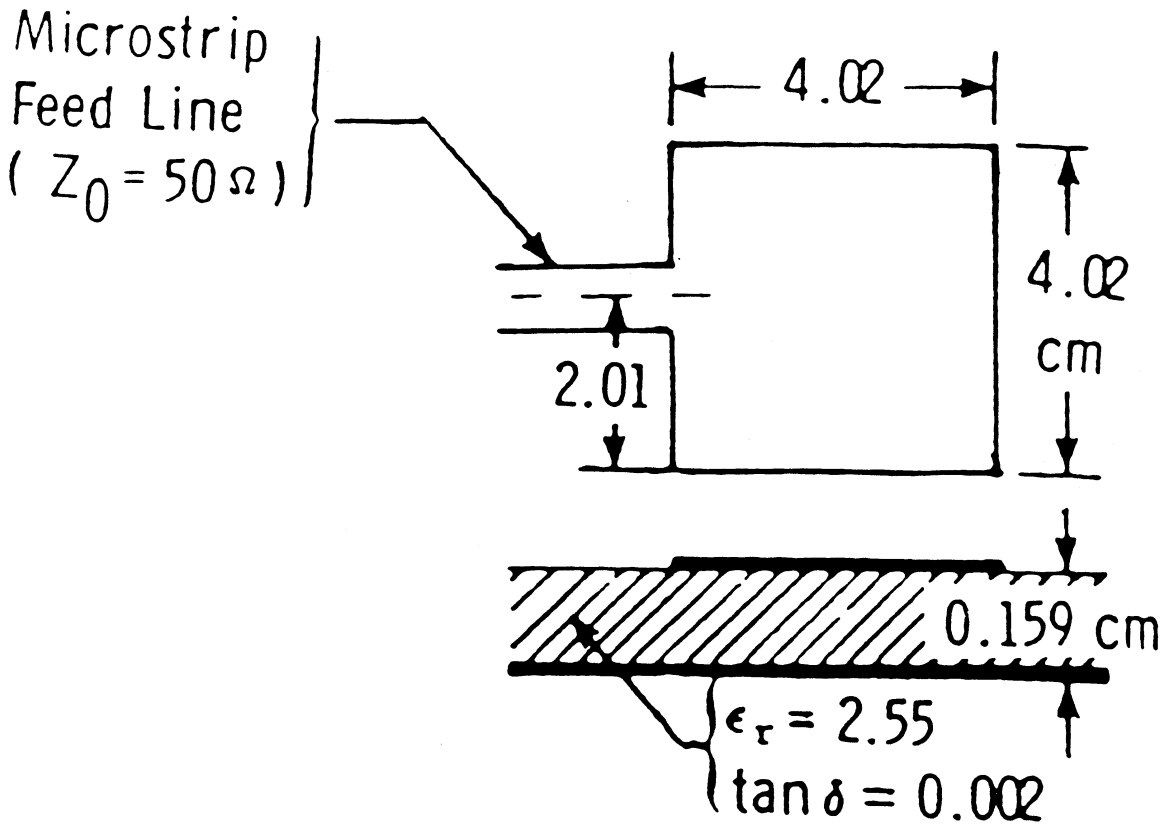

Figure 8. Geometry of the microstrip line-fed patch whose input impedance is given in Figure 9.

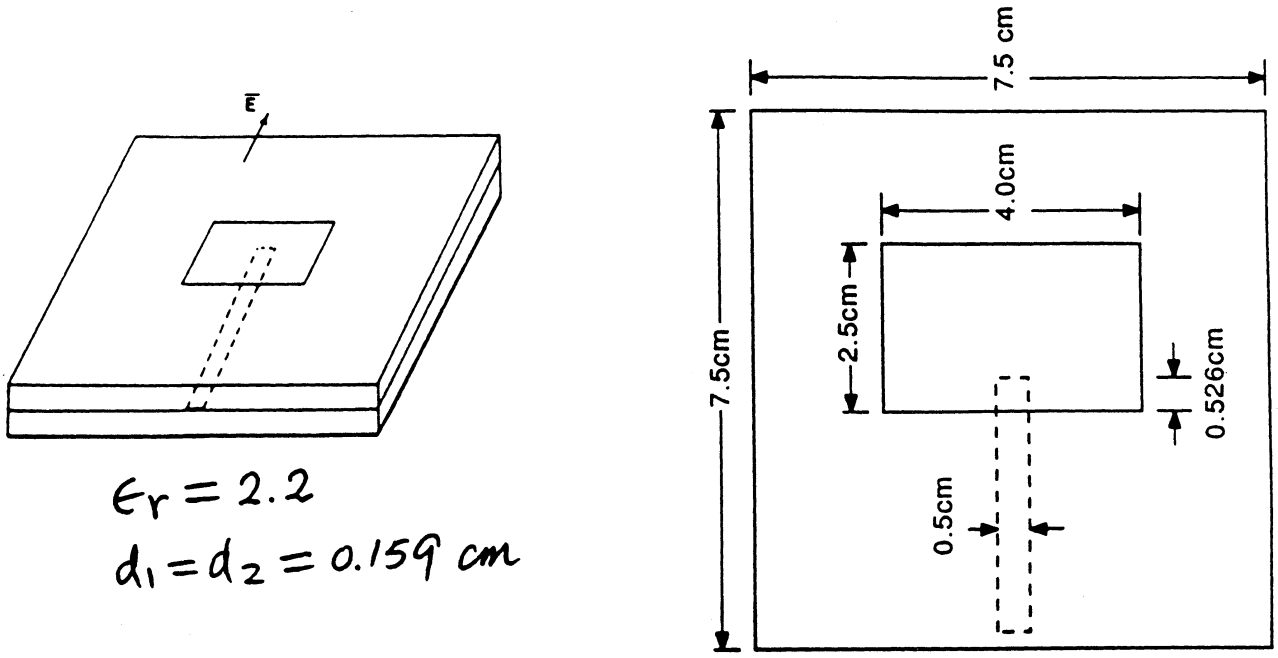

Figure 10. Geometry of the stripline-fed patch whose input impedance and reflection coefficient are shown in Figures 11 and 12. The substrate has $\epsilon_r = 2.2$ and the stripline is 0.159cm below the patch and 0.159cm above the ground plane.

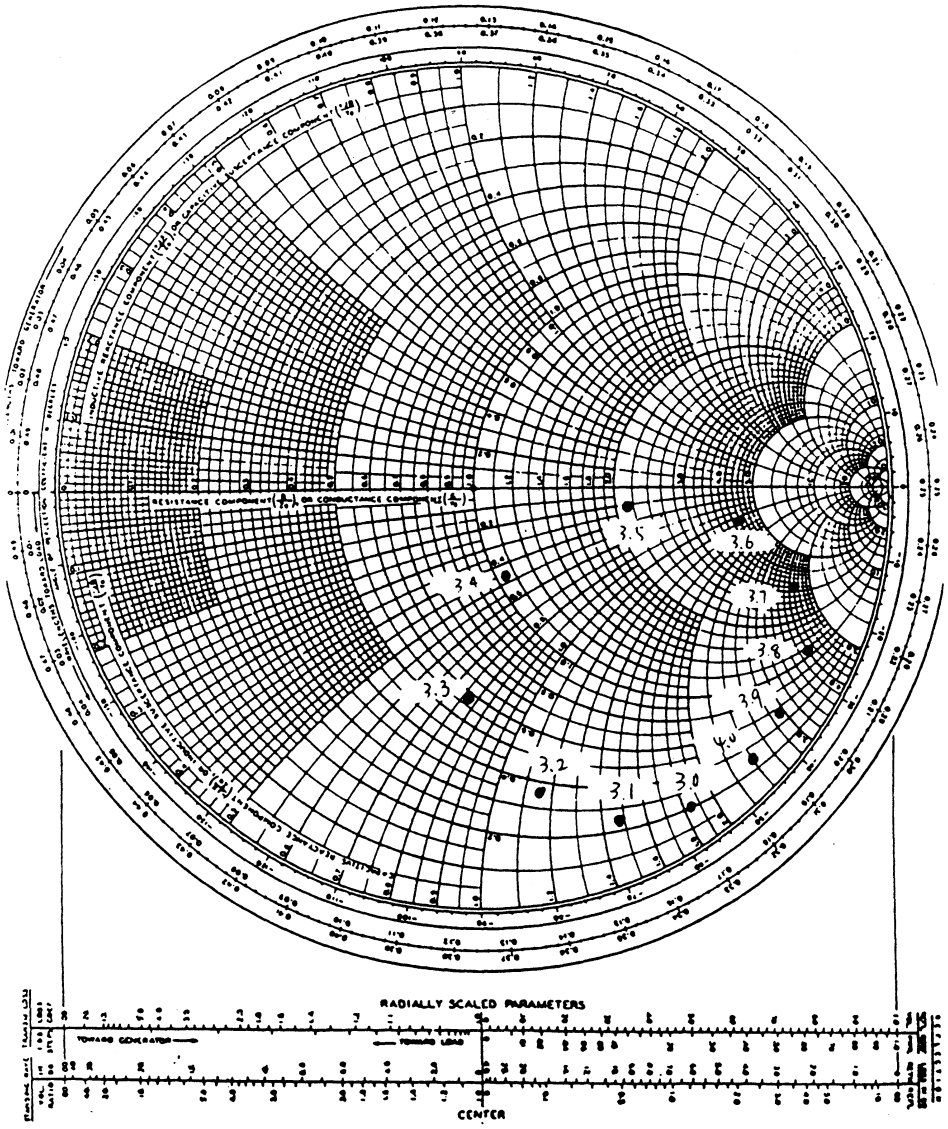

Figure 11. Calculated input impedance of the stripline-fed patch shown in Figure 10 at frequencies from 3.0GHz–4.0GHz. The impedance is referenced to point below the patch's edge.

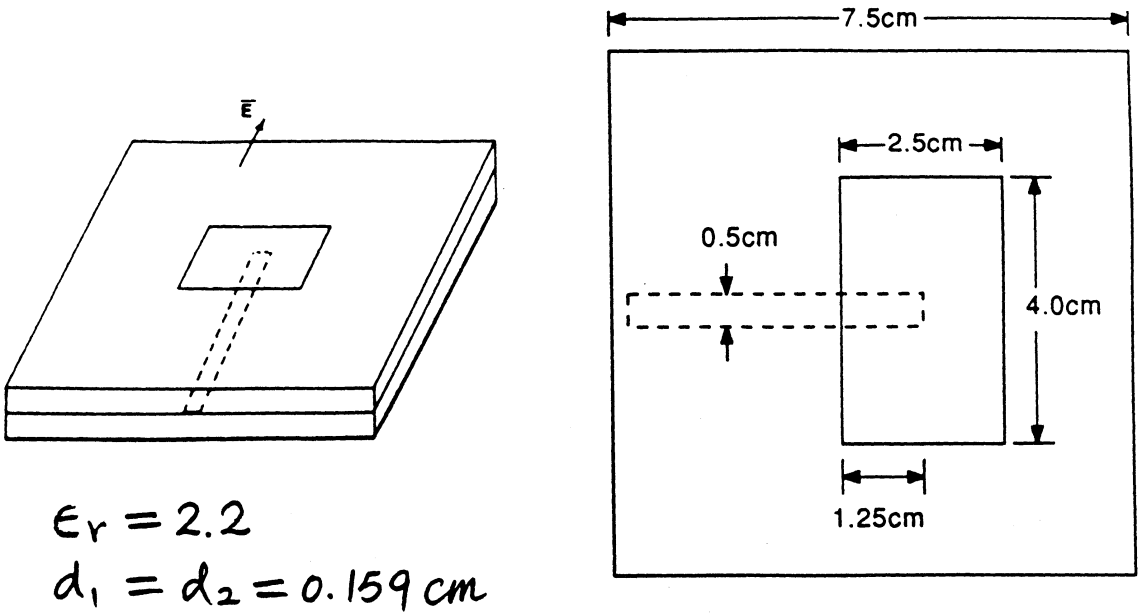

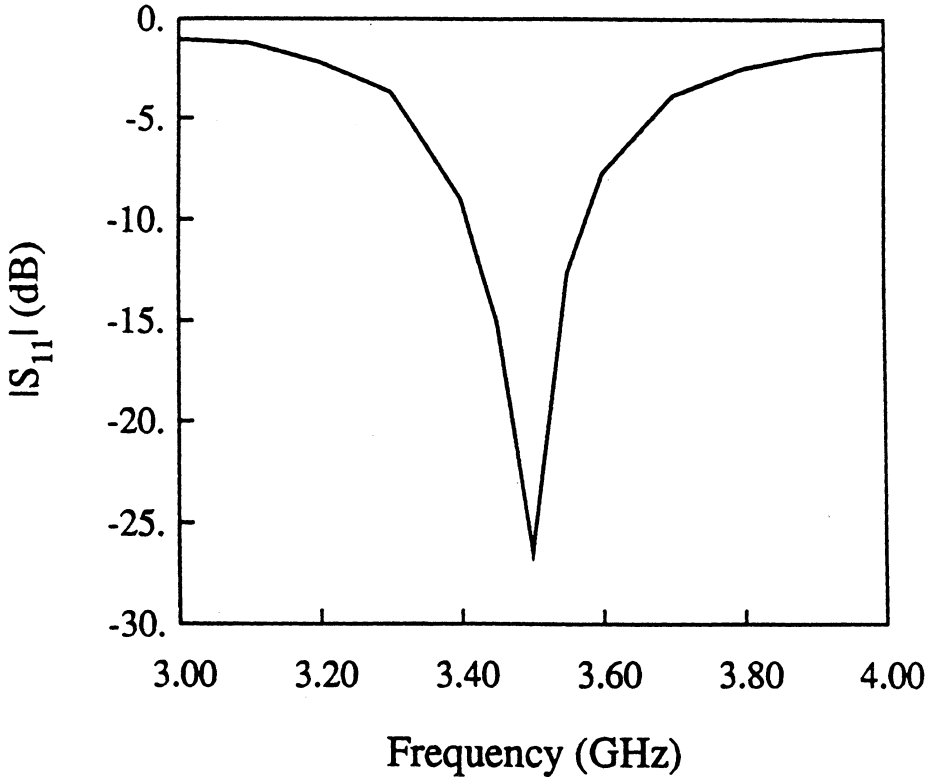

Figure 12. Calculated S_{11} scattering coefficient to the stripline-fed patch shown in Figure 10.

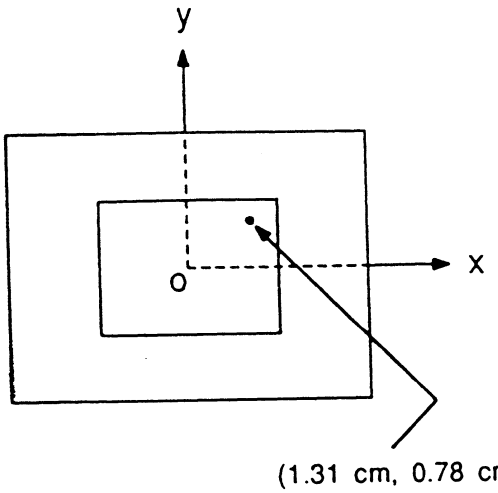

T=0.158 cm
ϵ_r=2.17
tanδ=0.001
N=1280
f=2.62 GHz

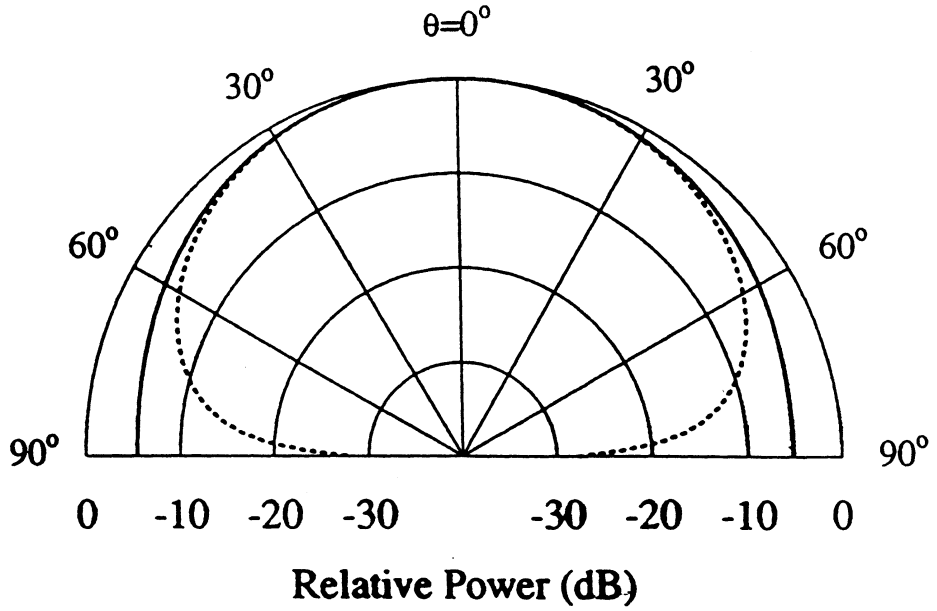

Calculated E and H plane radiatio pattern of the illustrated cavity-backed patch at 2.62GHz. The feed is at (1.31cm, 0.78cm), the patch size is 3.66cm × 2.60cm. The substrate is housed in a 7.32cm × 5.20cm × 0.158cm cavity.

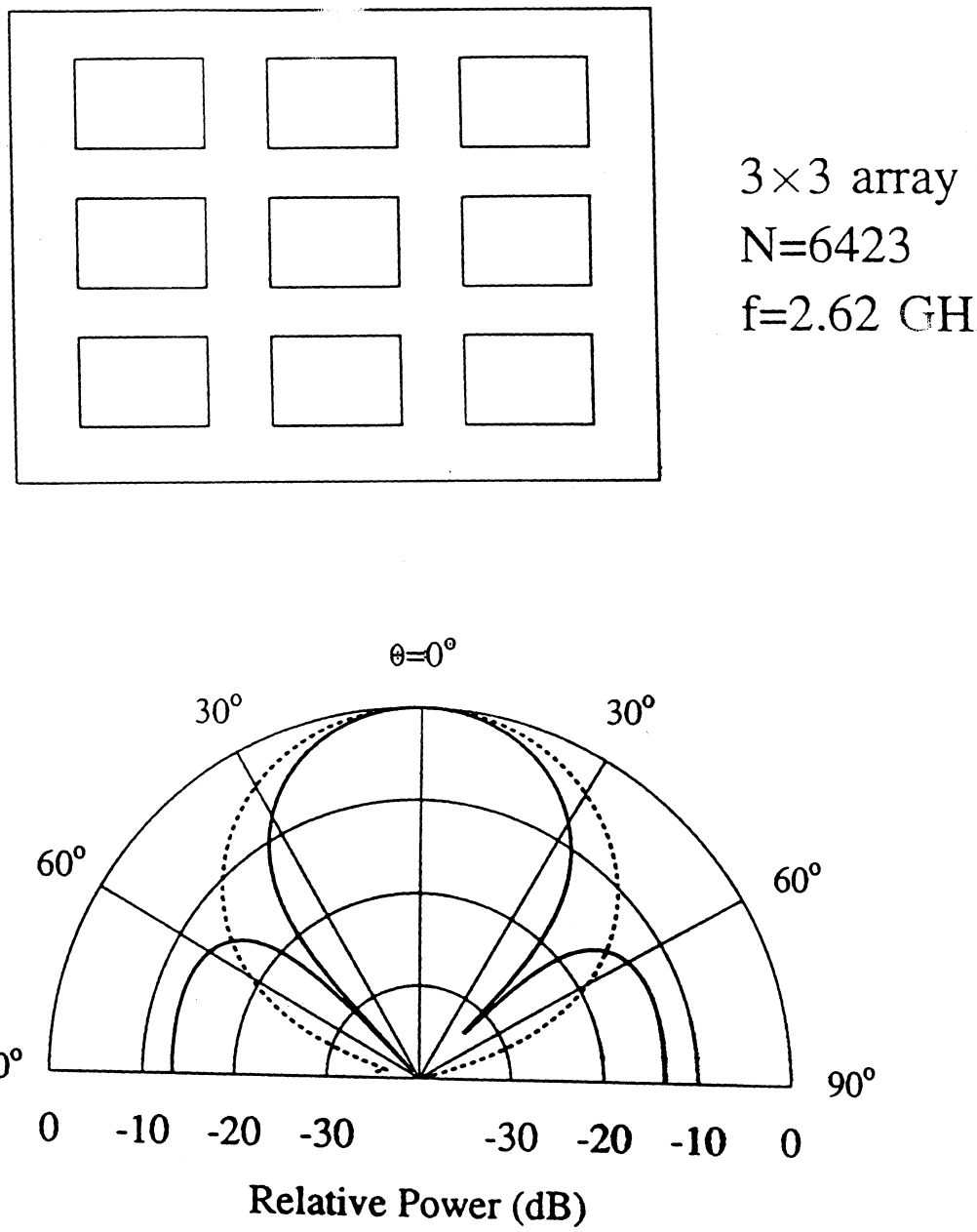

Figure 14. Calculated E and H plane radiation patterns of a 3 × 3 cavity-backed patch array at 2.62GHz. The patches are uniformly fed and identical in size to that in Figure 13. Their centers are 5.49cm apart in the x-direction and 3.90cm apart in the y-direction. The entire array is housed in 18.3cm × 13cm × 0.158cm cavity.

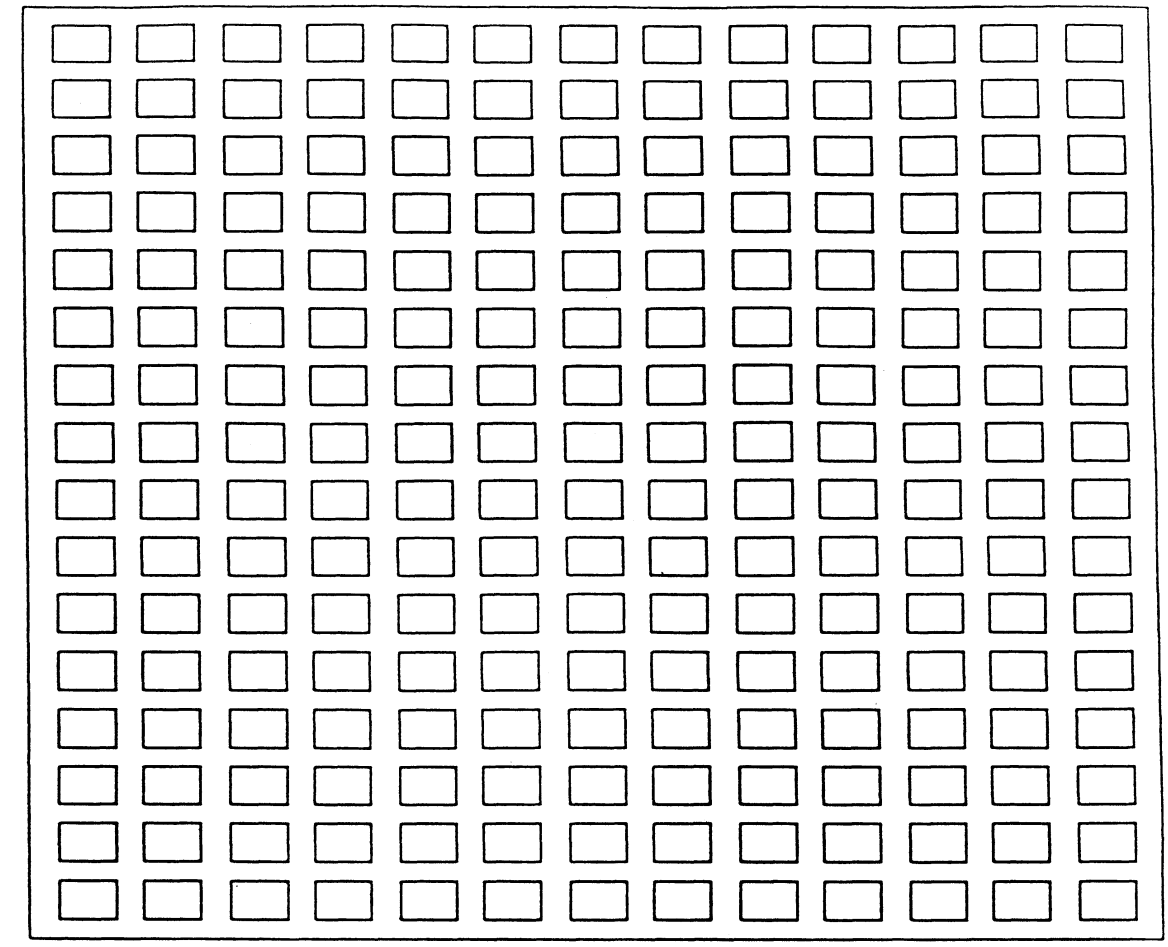

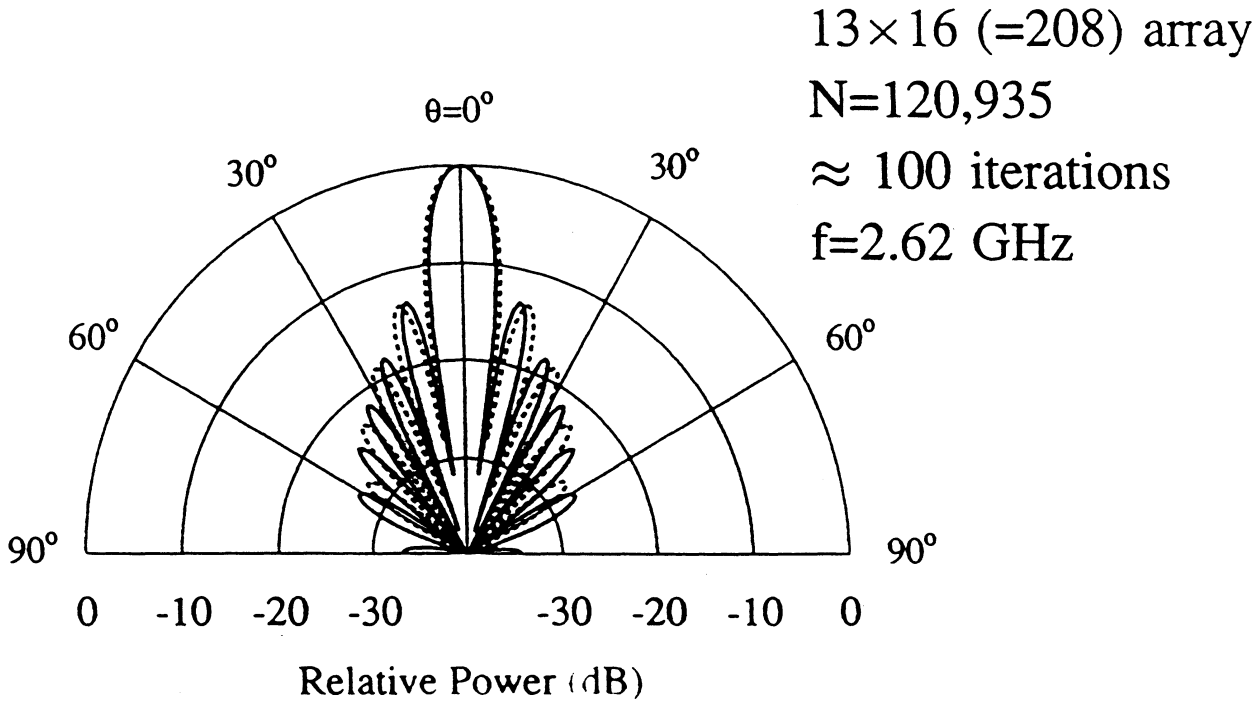

Figure 15. Calculated E and H plane radiation pattern of the illustrated 13 × 16 element array at 2.62GHz. Each patch is identical to that shown in Figure 13 and their separation is the same as that associated with array in Figure 14.

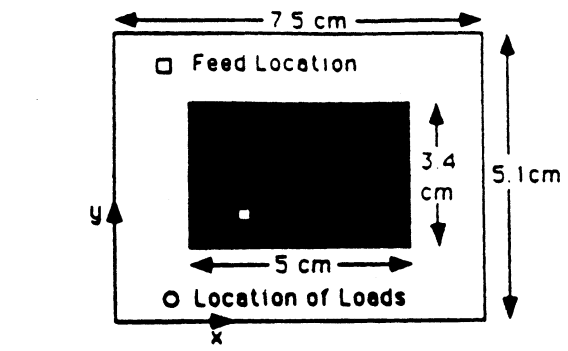

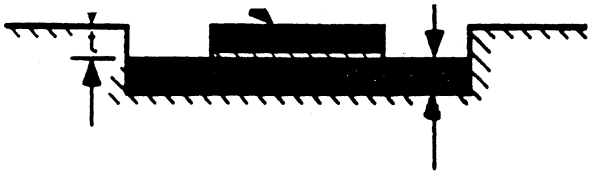

Figure 16. Geometry of the dielectrically coated patch. The coating has $\epsilon_r = 10.2 - j3.8$, $\mu_r = 2.12 - j1.5$. The lower substrate has $\epsilon_r = 2.17$.

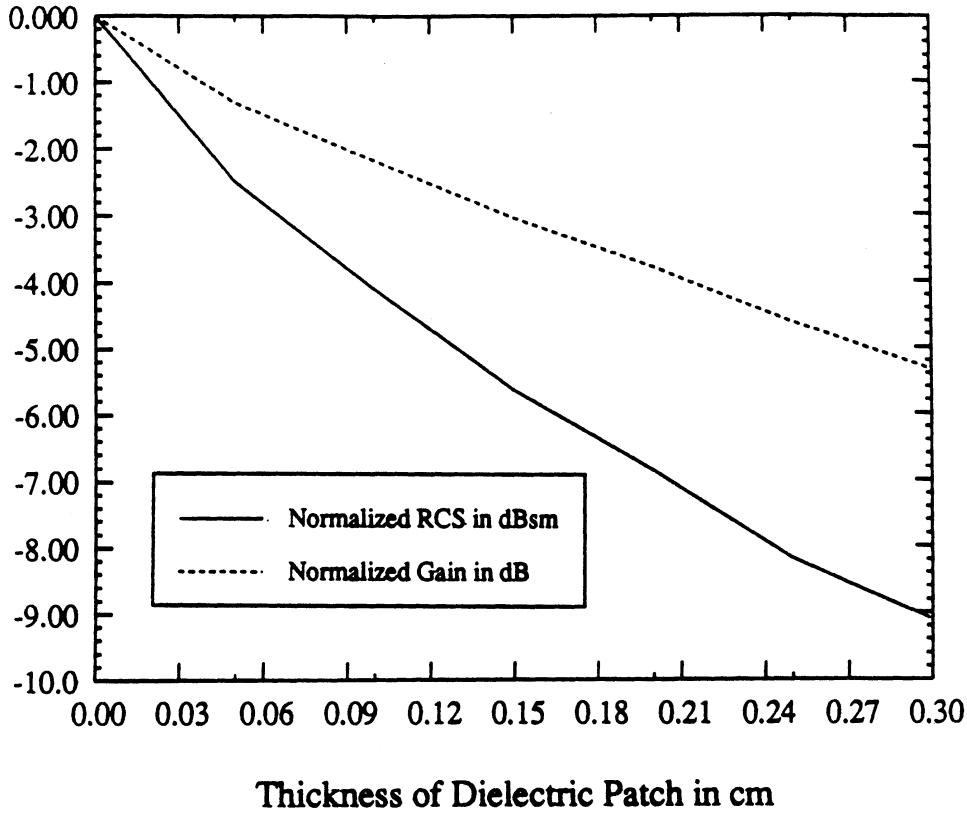

Figure 17. Normal incidence normalized RCS and Gain of the patch in Figure 15 as a function of coating thickness at the resonant frequency.

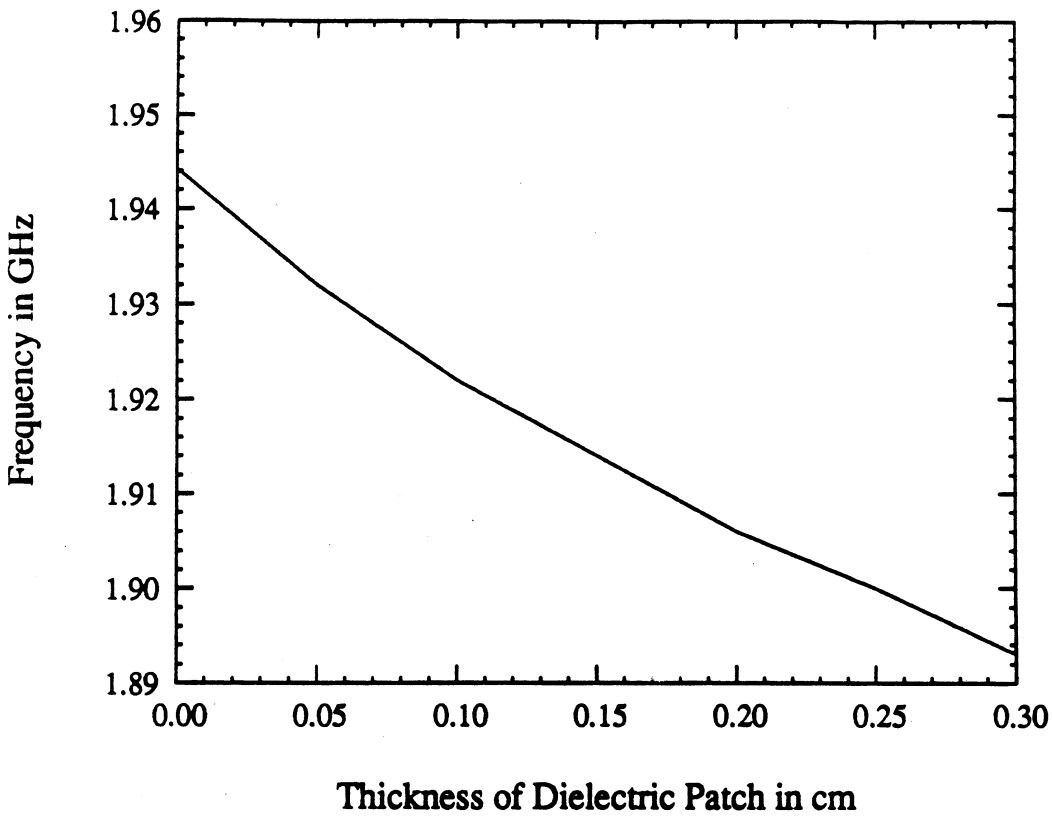

Figure 18. Resonant frequency of the coated patch in Figure 16 as a function of coating thickness.

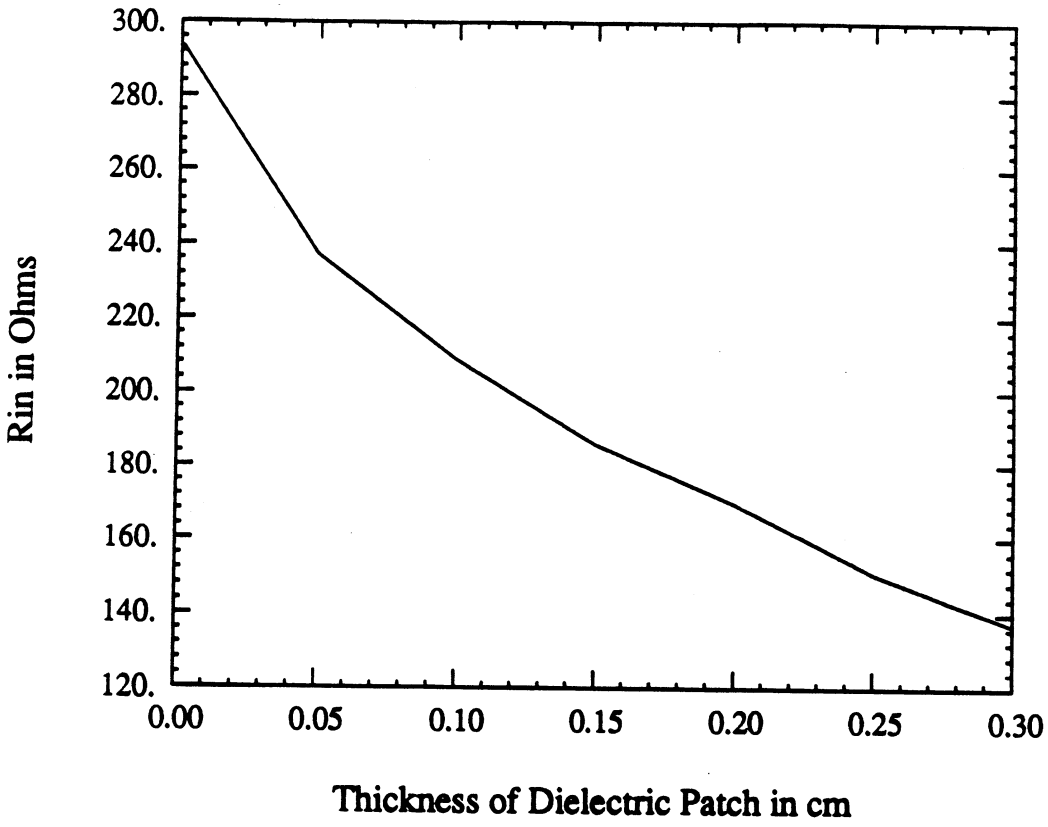

Figure 19. Input resistance of the coated patch in Figure 16 as a function of coating thickness.

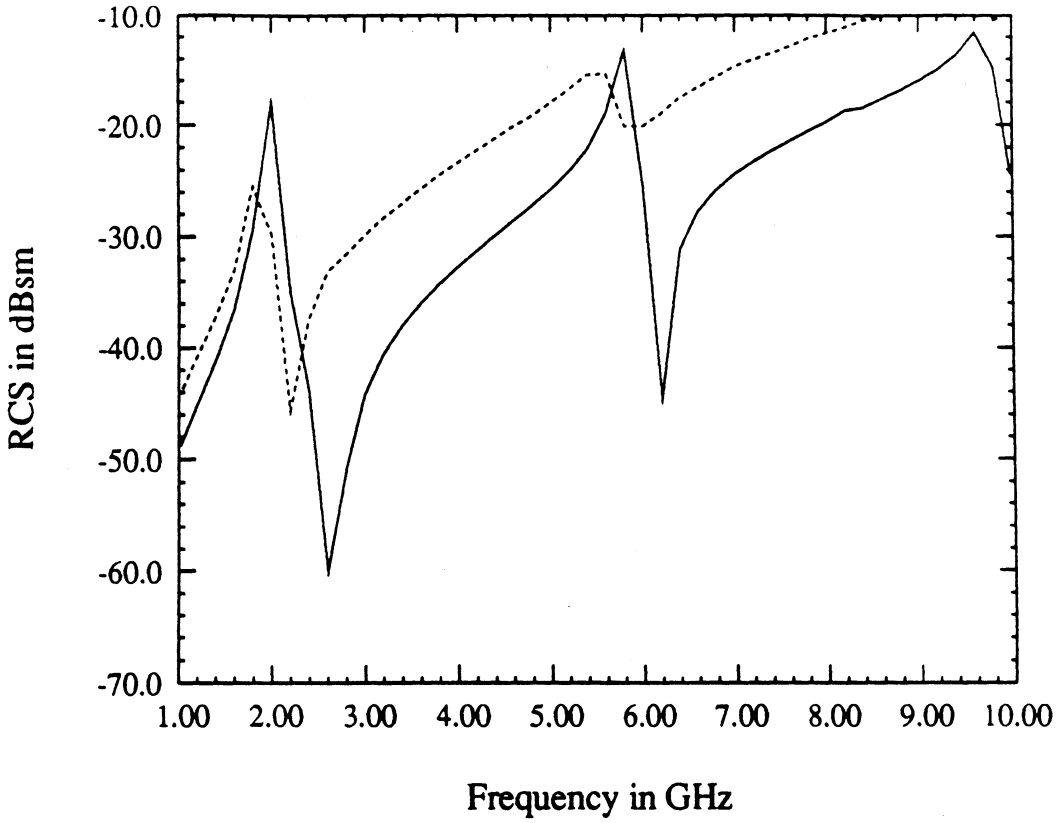

Figure 20. Normal incidence RCS of the coated patch in Figure 16 as a function of frequency. Comparison of data calculated with and without a coating of thickness 0.15cm.

RCS of a patch in a cavity with and w/o resistive loading at the edges

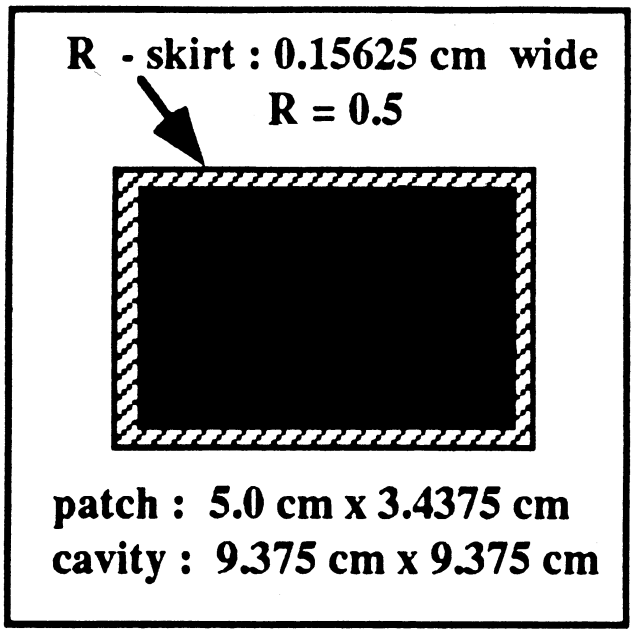

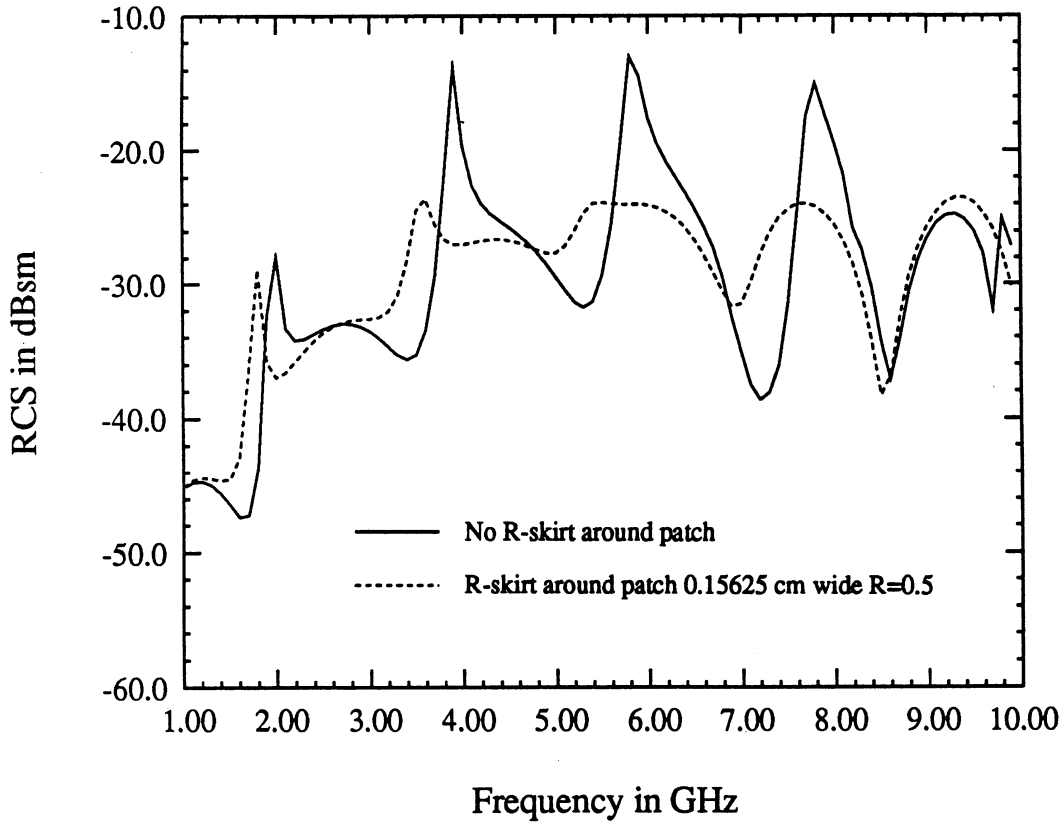

Figure 21. Geometry of the patch loaded with a resistive skirt at the edges and its backscatter RCS as a function of frequency. The RCS was computed at an incidence angle of 70 degrees from the normal.

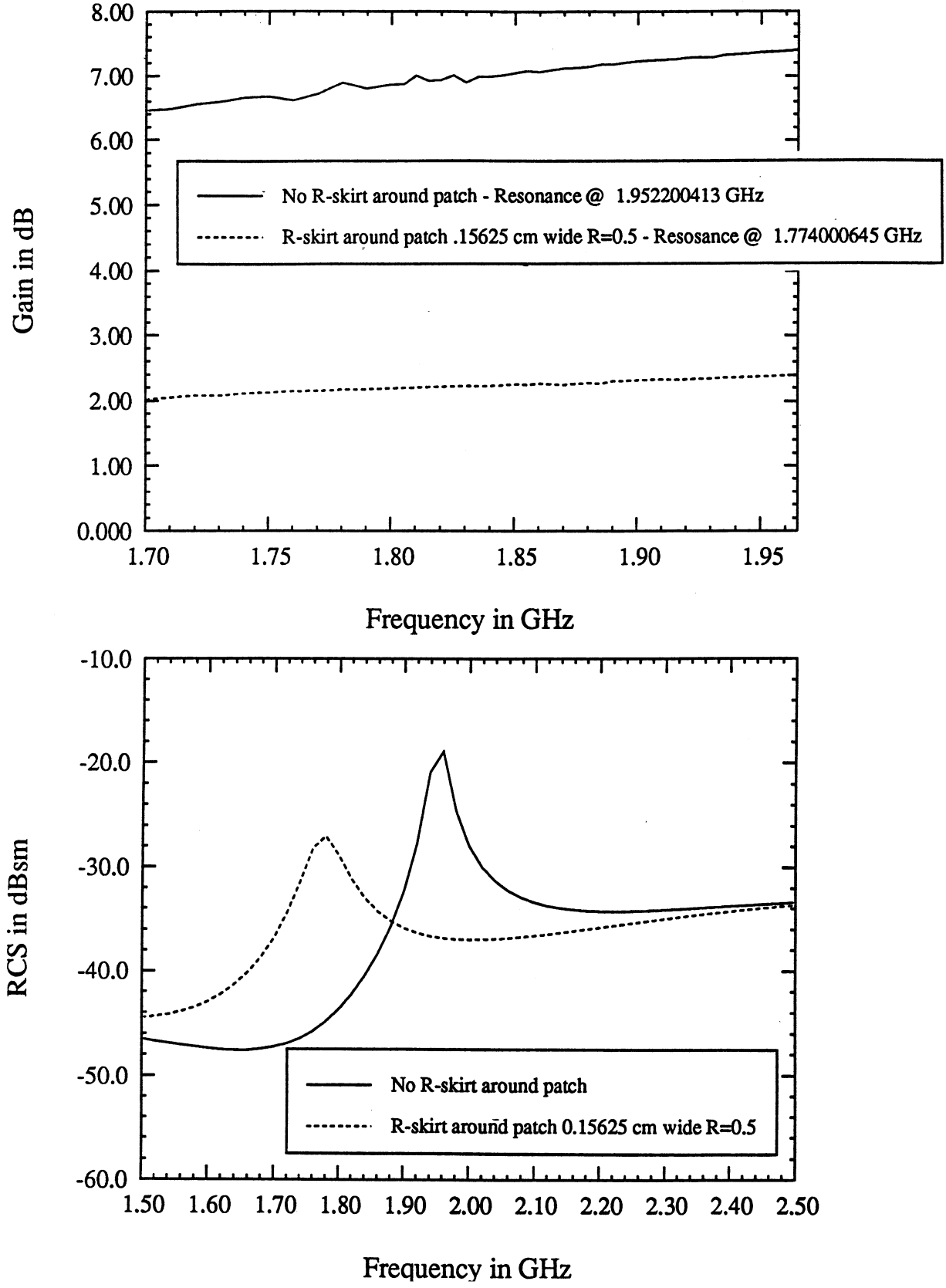

Figure 22. Gain and RCS of the patch in Figure 21 at near resonance.

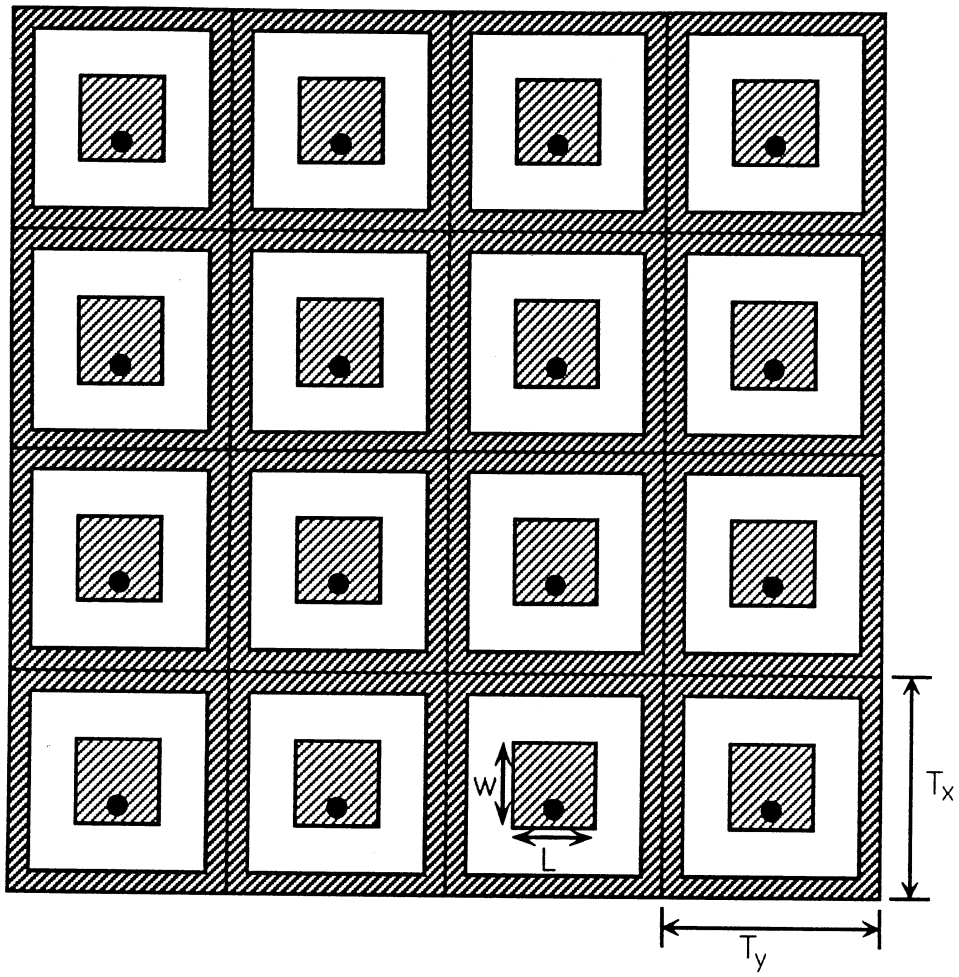

Figure 23. Array of patches residing on the surface of individual rectangular cavities.

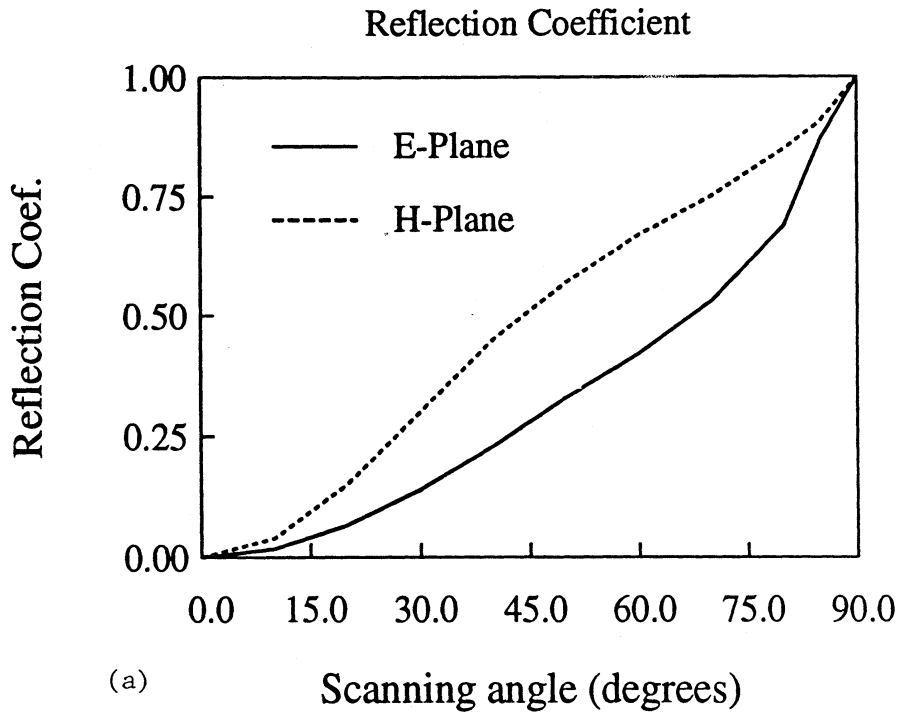

(a)

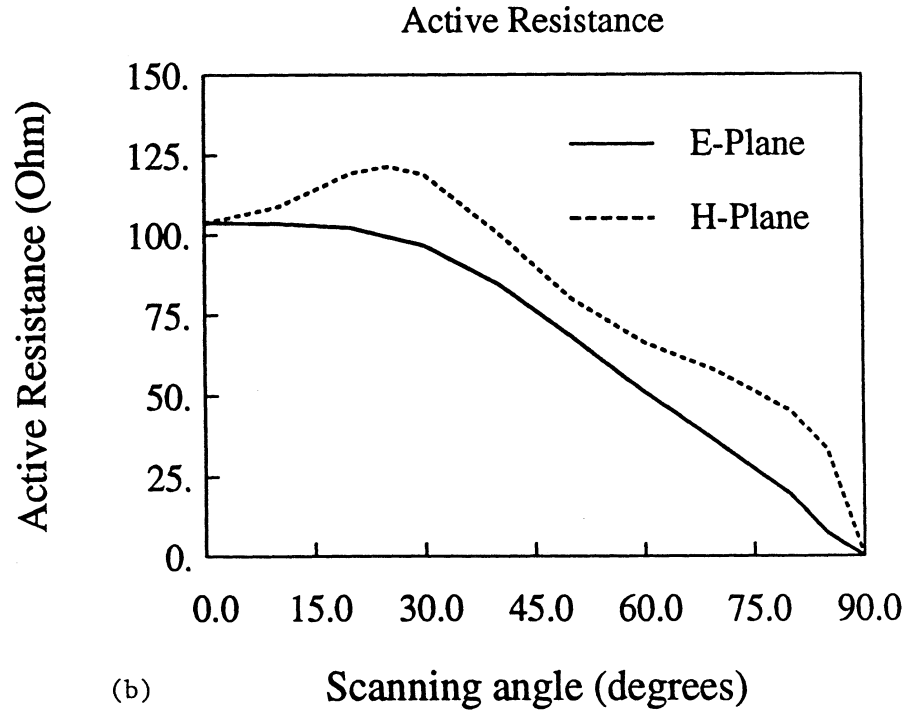

(b)

Figure 24. Reflection coefficient and active resistance as a function of scan angle for the 5×5 cavity-backed patch array in Figure 23. For this computation $T_x = T_y = 5$cm, the cavity size is 4.5cm $\times$ 4.5cm $\times$ 0.2cm, $f = 3$GHz and the patch size is 3cm $\times$ 3cm. Also, the cavity is filled with a dielectric having $\epsilon_r = 2.80$.

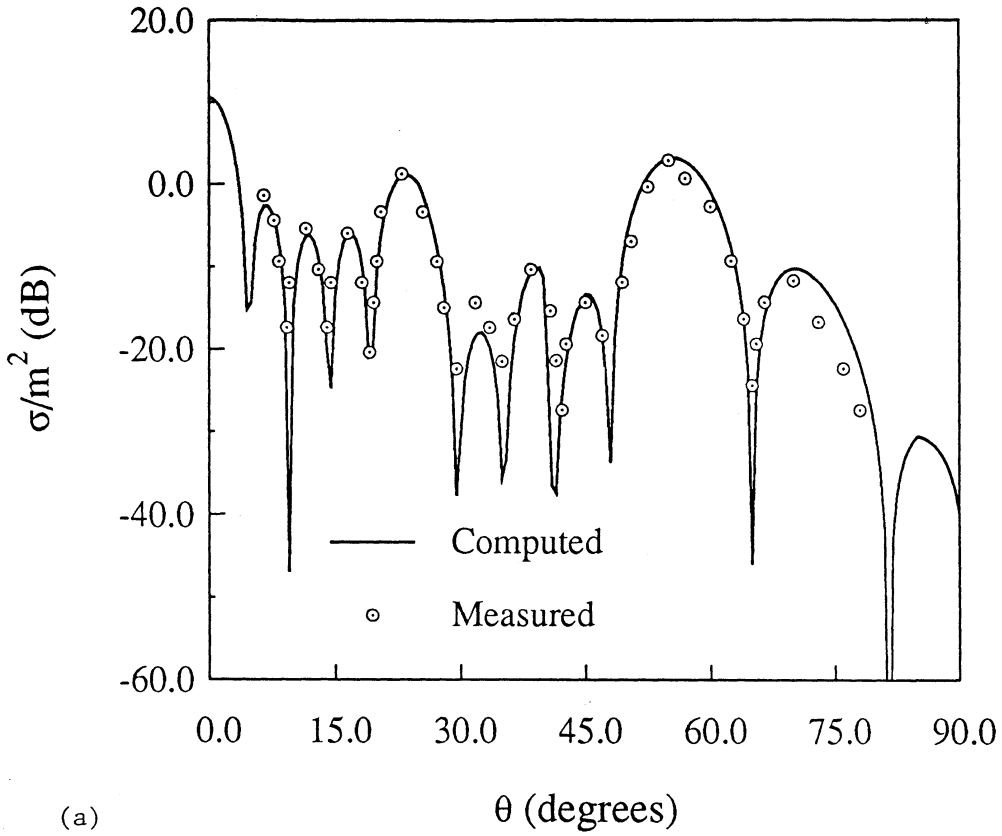

(a)

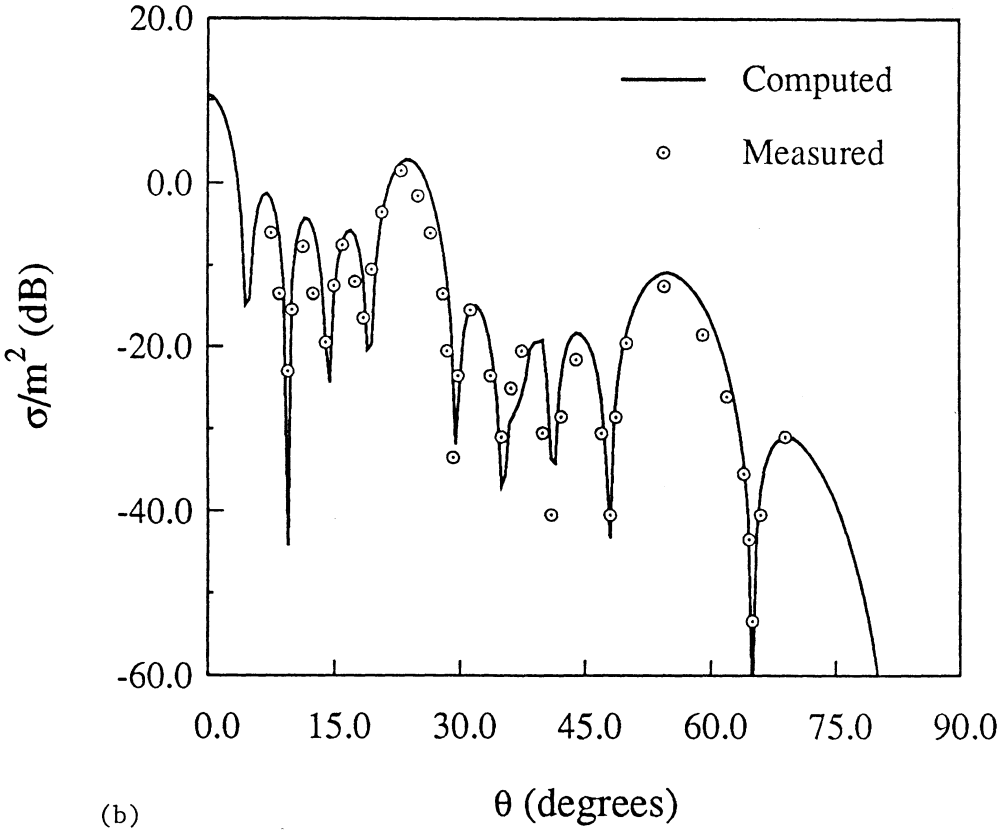

(b)

Figure 25. Principal backscatter pattern of the 5 × 5 cavity array shown in Figure 23 with the patch removed. For this computation $T_x = T_y = 4$cm, $d = 0.45$cm, and $f = 9.1$GHz. (a) E_θ pattern; (b) E_ϕ pattern.

Appendix 1

Discretization of the volume region

For a numerical implementation of (5) we must first discretize the functionals by subdividing V and S into smaller volume and surface elements, respectively. Considering (8), it is convenient to rewrite the functional F as

$$F = F_V + F_S + F_I + F_E \tag{A1}$$

where F_V is the volume integral

$$F_V = \frac{1}{2}\iiint_V \left\{ \frac{1}{\mu_r}\left[\left(\frac{\partial E_z}{\partial y} - \frac{\partial E_y}{\partial z}\right)^2 + \left(\frac{\partial E_x}{\partial z} - \frac{\partial E_z}{\partial x}\right)^2 + \left(\frac{\partial E_y}{\partial x} - \frac{\partial E_x}{\partial y}\right)^2\right] - k_0^2\epsilon_r\left(E_x^2 + E_y^2 + E_z^2\right)\right\} dV \tag{A2}$$

obtained by expanding the appropriate integrand in (8) and F_S denotes the surface integral

$$F_S = -2k_0^2 \iint_S \mathbf{M}(\mathbf{r}) \bullet \left[\iint_S \bar{\bar{\mathrm{G}}}_0(\mathbf{r},\mathbf{r}') \bullet \mathbf{M}(\mathbf{r}')\, dS'\right] dS. \tag{A3}$$

The remaining portion of F is associated with the sources and is given by

$$F_I = \iiint_V \left[jk_0 Z_0 \mathbf{J}_i \bullet \mathbf{E} - \frac{1}{\mu_r}\mathbf{M}_i \bullet (\nabla \times \mathbf{E})\right] dV \tag{A4}$$

and

$$F_E = -2jk_0 Z_0 \iint_S \mathbf{M}(\mathbf{r}) \bullet \mathbf{H}^i(\mathbf{r})\, dS \tag{A5}$$

upon using the relation $\hat{\mathbf{z}} \times \mathbf{H}^r(\mathbf{r}) = \hat{\mathbf{z}} \times \mathbf{H}^i(\mathbf{r})$. For simplicity, we have omitted the superscript II and this practice will be continued in the remaining portion of the report.

To discretize (A2) we subdivide the volume V into M_v small volume elements such as tetrahedra, triangular prisms, or rectangular bricks. The ideal element for the discretization of rectangular cavities or those that can be modelled as a collection of rectangular volumes is the rectangular brick illustrated in Figure A1. For arbitrarily shaped cavities, triangular prisms and tetrahedra may be used but in this report we restrict our attention to rectangular bricks. Consider the rectangular brick of dimensions $a \times b \times c$, representing the eth element, as illustrated in Figure A1. The field components within this element may be expressed as

$$E_x = \sum_{j=1}^{4} N_{xj}^e(y,z)\,\phi_{xj}^e \; ; \quad E_y = \sum_{j=1}^{4} N_{yj}^e(z,x)\,\phi_{yj}^e \; ; \quad E_z = \sum_{j=1}^{4} N_{zj}^e(x,y)\,\phi_{zj}^e \tag{A6}$$

where N_{xj}^e, N_{yj}^e and N_{zj}^e are the expansion or shape functions given by

$$N_{x1}^e = \tfrac{(b-y')(c-z')}{bc} \; ; \quad N_{x2}^e = \tfrac{y'(c-z')}{bc} \; ; \quad N_{x3}^e = \tfrac{(b-y')z'}{bc} \; ; \quad N_{x4}^e = \tfrac{y'z'}{bc}$$

$$N_{y1}^e = \tfrac{(c-z')(a-x')}{ca} \; ; \quad N_{y2}^e = \tfrac{z'(a-x')}{ca} \; ; \quad N_{y3}^e = \tfrac{(c-z')x'}{ca} \; ; \quad N_{y4}^e = \tfrac{z'x'}{ca}$$

$$N_{z1}^e = \tfrac{(a-x')(b-y')}{ab} \; ; \quad N_{z2}^e = \tfrac{x'(b-y')}{ab} \; ; \quad N_{z3}^e = \tfrac{(a-x')y'}{ab} \; ; \quad N_{z4}^e = \tfrac{x'y'}{ab} \quad .$$

In these, (x', y', z') denote the local coordinates specifying a point within the eth element and from an examination of the expansion functions we observe that ϕ_{x1}^e represents an average of the field component E_x along the

edge segment (1,2). Likewise, ϕ^e_{x2} is associated with the E_x component along the edge (3,4), ϕ^e_{x3} corresponds to the E_x component along the edge (5,6) and ϕ^e_{x4} is associated with the E_x component along the edge (7,8). Similar identifications can, of course, be made for ϕ^e_{yj} and ϕ^e_{zj}. Therefore, N^e_{xj}, N^e_{yj} and N^e_{zj} can be termed as edge-based expansion functions, in contrast to the traditional node-based expansion functions. A feature of these functions is that they satisfy the divergence condition within the volume of the element and this permits the elimination of the usual penalty term. Also, the edge-based functions allow a convenient enforcement of the required boundary conditions at the dielectric interfaces and conducting walls. Furthermore, the edge-based functions avoid an explicit specification of the fields at the corners and edges, where these may be singular. This is not, however, permitted when employing the node-based expansion functions unless special basis functions (which model the singular behavior of the fields) are incorporated into the formulation leading to a much more complicated implementation.

Substituting (A6) into (A2) yields the portion of F_V attributed to the eth element. The complete expression for F_V is then obtained by summing/assembling the contributions from all elements. This yields a functional in terms of the unknown field components which must be found to satisfy (5). In accordance with the Rayleigh-Ritz procedure this is equivalent to setting the derivatives of F with respect to the fields ϕ^e_{pj} $(p = x, y, z)$ equal to zero.

Differentiating the portion of F_V attributed to the eth element with respect to the field ϕ^e_{xi} we obtain

$$\frac{\partial F^e_V}{\partial \phi^e_{xi}} = \sum_{j=1}^{4} \iiint_{V^e} \frac{1}{\mu_r} \left\{ \left[\frac{\partial N^e_{xi}}{\partial y}\frac{\partial N^e_{xj}}{\partial y} + \frac{\partial N^e_{xi}}{\partial z}\frac{\partial N^e_{xj}}{\partial z} - k_0^2 \epsilon_r \mu_r N^e_{xi} N^e_{xj} \right] \phi^e_{xj} - \frac{\partial N^e_{xi}}{\partial y}\frac{\partial N^e_{yj}}{\partial x}\phi^e_{yj} - \frac{\partial N^e_{xi}}{\partial z}\frac{\partial N^e_{zj}}{\partial x}\phi^e_{zj} \right\} dV. \quad \text{(A7)}$$

Similarly, by differentiating with respect to the other field components we have

$$\frac{\partial F^e_V}{\partial \phi^e_{yi}} = \sum_{j=1}^{4} \iiint_{V^e} \frac{1}{\mu_r} \left\{ -\frac{\partial N^e_{yi}}{\partial x}\frac{\partial N^e_{xj}}{\partial y}\phi^e_{xj} + \left[\frac{\partial N^e_{yi}}{\partial x}\frac{\partial N^e_{yj}}{\partial x} + \frac{\partial N^e_{yi}}{\partial z}\frac{\partial N^e_{yj}}{\partial z} - k_0^2 \epsilon_r \mu_r N^e_{yi} N^e_{yj} \right] \phi^e_{yj} - \frac{\partial N^e_{yi}}{\partial z}\frac{\partial N^e_{zj}}{\partial y}\phi^e_{zj} \right\} dV \quad \text{(A8)}$$

and

$$\frac{\partial F^e_V}{\partial \phi^e_{zi}} = \sum_{j=1}^{4} \iiint_{V^e} \frac{1}{\mu_r} \left\{ -\frac{\partial N^e_{zi}}{\partial x}\frac{\partial N^e_{xj}}{\partial z}\phi^e_{xj} - \frac{\partial N^e_{zi}}{\partial y}\frac{\partial N^e_{yj}}{\partial z}\phi^e_{yj} + \left[\frac{\partial N^e_{zi}}{\partial x}\frac{\partial N^e_{zj}}{\partial x} + \frac{\partial N^e_{zi}}{\partial y}\frac{\partial N^e_{zj}}{\partial y} - k_0^2 \epsilon_r \mu_r N^e_{zi} N^e_{zj} \right] \phi^e_{zj} \right\} dV. \quad \text{(A9)}$$

We observe that if ϵ_r and μ_r are assumed constant within the eth element, all integrals in (A7)–(A9) can be evaluated analytically. The results of this evaluation are as follows:

Let

$$(K_p^{00})_{ij} = \iiint_{V^e} N^e_{pi} N^e_{pj}\, dV \qquad p = x, y, z.$$

Then

$$[K_p^{00}] = \frac{abc}{36}\begin{bmatrix} 4 & 2 & 2 & 1 \\ 2 & 4 & 1 & 2 \\ 2 & 1 & 4 & 2 \\ 1 & 2 & 2 & 4 \end{bmatrix}$$

To evaluate

$$(K_p^{qq})_{ij} = \iiint_{V^e} \frac{\partial N_{pi}^e}{\partial q}\frac{\partial N_{pj}^e}{\partial q}\, dV \qquad p = x, y, z, \quad q = x, y, z$$

let

$$[K_1] = \begin{bmatrix} 2 & -2 & 1 & -1 \\ -2 & 2 & -1 & 1 \\ 1 & -1 & 2 & -2 \\ -1 & 1 & -2 & 2 \end{bmatrix}$$

and

$$[K_2] = \begin{bmatrix} 2 & 1 & -2 & -1 \\ 1 & 2 & -1 & -2 \\ -2 & -1 & 2 & 1 \\ -1 & -2 & 1 & 2 \end{bmatrix}$$

In terms of these submatrices we find

$$[K_x^{yy}] = \frac{ac}{6b}[K_1], \quad [K_x^{zz}] = \frac{ab}{6c}[K_2]$$
$$[K_y^{zz}] = \frac{ab}{6c}[K_1], \quad [K_y^{xx}] = \frac{bc}{6a}[K_2]$$
$$[K_z^{xx}] = \frac{bc}{6a}[K_1], \quad [K_z^{yy}] = \frac{ac}{6b}[K_2]$$

To evaluate

$$(K_{pq}^{qp})_{ij} = \iiint_{V^e} \frac{\partial N_{pi}^e}{\partial q}\frac{\partial N_{qj}^e}{\partial p}\, dV \qquad p = x, y, z, \quad q = x, y, z$$

let

$$[K_3] = \begin{bmatrix} 2 & 1 & -2 & -1 \\ -2 & -1 & 2 & 1 \\ 1 & 2 & -1 & -2 \\ -1 & -2 & 1 & 2 \end{bmatrix}$$

Then

$$[K_{xy}^{yx}] = \frac{c}{6}[K_3], \quad [K_{yz}^{zy}] = \frac{a}{6}[K_3], \quad [K_{zx}^{xz}] = \frac{b}{6}[K_3],$$

and other elements are given by

$$[K_{pq}^{qp}] = [K_{qp}^{pq}]^T.$$

Discretization of the boundary equation

Let us now consider the discretization of the surface integral in (A3). A difficulty in the evaluation of this integral is the usual singularity associated with the derivatives of the free space Green's function. This, however, can be avoided by transfering the derivatives to the current. To do so, we invoke a common vector identity and the divergence theorem, leading to

$$\begin{aligned} F_S &= -2 \iint_S \mathbf{M}(\mathbf{r}) \bullet \left[k_0^2 \iint_S \mathbf{M}(\mathbf{r}') G_0(\mathbf{r}, \mathbf{r}')\, dS' \right. \\ &\qquad \left. + \nabla \iint_S \nabla' \bullet \mathbf{M}(\mathbf{r}') G_0(\mathbf{r}, \mathbf{r}')\, dS' \right] dS. \end{aligned} \tag{A10}$$

Through the same process, (A10) can be further rewritten as

$$\begin{aligned} F_S &= -2k_0^2 \iint_S \mathbf{M}(\mathbf{r}) \bullet \left[\iint_S \mathbf{M}(\mathbf{r}') G_0(\mathbf{r}, \mathbf{r}')\, dS' \right] dS \\ &\qquad + 2 \iint_S \nabla \bullet \mathbf{M}(\mathbf{r}) \left[\iint_S \nabla' \bullet \mathbf{M}(\mathbf{r}') G_0(\mathbf{r}, \mathbf{r}')\, dS' \right] dS, \end{aligned} \tag{A11}$$

and by invoking (1) we obtain

$$\begin{aligned} F_S &= -2k_0^2 \iint_S E_x \left[\iint_S E_x G_0\, dS' \right] dS - 2k_0^2 \iint_S E_y \left[\iint_S E_y G_0\, dS' \right] dS \\ &\qquad + 2 \iint_S \left(\frac{\partial E_x}{\partial y} - \frac{\partial E_y}{\partial x} \right) \left[\iint_S \left(\frac{\partial E_x}{\partial y'} - \frac{\partial E_y}{\partial x'} \right) G_0\, dS' \right] dS, \end{aligned} \tag{A12}$$

which can be discretized by subdividing S into M_s smaller surface elements. Substituting (A6) into (A12) and replacing S in the first pair of integrals with S^e, the area of the eth surface element, gives the portion of F_S attributed to the eth element. As noted earlier, to enforce the stationarity condition we need the derivatives of F_S with respect to the fields ϕ^e_{xi} and ϕ^e_{yi}. For the eth element we have

$$\frac{\partial F^e_S}{\partial \phi^e_{xi}} = -2k_0^2 \iint_{S^e} N^e_{xi} \left[\sum_{e=1}^{M_s} \sum_{j=1}^{2} \phi^e_{xj} \iint_{S^e} N^e_{xj} G_0 \, dS' \right] dS \tag{A13}$$
$$+ 2 \iint_{S^e} \frac{\partial N^e_{xi}}{\partial y} \left[\sum_{e=1}^{M_s} \sum_{j=1}^{2} \iint_{S^e} \left(\frac{\partial N^e_{xj}}{\partial y'} \phi^e_{xj} - \frac{\partial N^e_{yj}}{\partial x'} \phi^e_{yj} \right) G_0 \, dS' \right] dS,$$

$$\frac{\partial F^e_S}{\partial \phi^e_{yi}} = -2k_0^2 \iint_{S^e} N^e_{yi} \left[\sum_{e=1}^{M_s} \sum_{j=1}^{2} \phi^e_{yj} \iint_{S^e} N^e_{yj} G_0 \, dS' \right] dS \tag{A14}$$
$$- 2 \iint_{S^e} \frac{\partial N^e_{yi}}{\partial x} \left[\sum_{e=1}^{M_s} \sum_{j=1}^{2} \iint_{S^e} \left(\frac{\partial N^e_{xj}}{\partial y'} \phi^e_{xj} - \frac{\partial N^e_{yj}}{\partial x'} \phi^e_{yj} \right) G_0 \, dS' \right] dS,$$

and $\partial F^e_S / \partial \phi^e_{zi} = 0$ since F_S is not a function of E_z. We note that in deriving (A13) and (A14) the differentiation was performed only with respect to the node fields outside the square brackets in (A12) while those introduced by substituting (2) into (6) remained unaffected.

It remains to discretize (A4) and (A5) which involve the excitation fields. Let us consider (A4) first. By expanding the integrand in (A4), we have

$$F_I = jk_0 Z_0 \iiint_V (E_x J_{ix} + E_y J_{iy} + E_z J_{iz}) \, dV - \iiint_V \frac{1}{\mu_r} \left[\left(\frac{\partial E_z}{\partial y} - \frac{\partial E_y}{\partial z} \right) M_{ix} \right.$$
$$\left. + \left(\frac{\partial E_x}{\partial z} - \frac{\partial E_z}{\partial x} \right) M_{iy} + \left(\frac{\partial E_y}{\partial x} - \frac{\partial E_x}{\partial y} \right) M_{iz} \right] dV. \tag{A15}$$

By introducing the expansion (16), we obtain

$$\frac{\partial F_I^e}{\partial \phi_{xi}^e} = jk_0 Z_0 \iiint_{V^e} N_{xi}^e J_{ix}\, dV - \iiint_{V^e} \frac{1}{\mu_r}\left(\frac{\partial N_{xi}}{\partial z} M_{iy} - \frac{\partial N_{xi}}{\partial y} M_{iz}\right) dV, \quad \text{(A16)}$$

$$\frac{\partial F_I^e}{\partial \phi_{yi}^e} = jk_0 Z_0 \iiint_{V^e} N_{yi}^e J_{iy}\, dV - \iiint_{V^e} \frac{1}{\mu_r}\left(\frac{\partial N_{yi}}{\partial x} M_{iz} - \frac{\partial N_{yi}}{\partial z} M_{ix}\right) dV, \quad \text{(A17)}$$

and

$$\frac{\partial F_I^e}{\partial \phi_{zi}^e} = jk_0 Z_0 \iiint_{V^e} N_{zi}^e J_{iz}\, dV - \iiint_{V^e} \frac{1}{\mu_r}\left(\frac{\partial N_{zi}}{\partial y} M_{ix} - \frac{\partial N_{zi}}{\partial x} M_{iy}\right) dV. \quad \text{(A18)}$$

Now let us consider (A5). By replacing $\mathbf{M}$ with $\mathbf{E}$ in accordance with (1) we obtain

$$F_E = 2jk_0 Z_0 \iint_S \left(E_x H_y^i - E_y H_x^i\right) dS. \quad \text{(A19)}$$

This can again be discretized by introducing the expansion (A6), and by doing so we obtain (for the eth element)

$$\frac{\partial F_E^e}{\partial \phi_{xi}^e} = 2jk_0 Z_0 \iint_{S^e} N_{xi}^e H_y^i\, dS \quad \text{(A20)}$$

and

$$\frac{\partial F_E^e}{\partial \phi_{yi}^e} = -2jk_0 Z_0 \iint_{S^e} N_{yi}^e H_x^i\, dS. \quad \text{(A21)}$$

Given the partial derivatives of all integral functions comprising the functional F we can now proceed with the construction of the final system of

equations by imposing the stationarity condition (5). This implies that

$$\frac{\partial F}{\partial \phi_{xi}} = \sum_{e=1}^{M_v} \frac{\partial F_V^e}{\partial \phi_{xi}^e} + \sum_{e=1}^{M_v} \frac{\partial F_I^e}{\partial \phi_{xi}^e} + \sum_{e=1}^{M_s} \frac{\partial F_S^e}{\partial \phi_{xi}^e} + \sum_{e=1}^{M_s} \frac{\partial F_E^e}{\partial \phi_{xi}^e} = 0 \qquad \text{(A22)}$$

$$i = 1, 2, 3, ..., N_x$$

$$\frac{\partial F}{\partial \phi_{yi}} = \sum_{e=1}^{M_v} \frac{\partial F_V^e}{\partial \phi_{yi}^e} + \sum_{e=1}^{M_v} \frac{\partial F_I^e}{\partial \phi_{yi}^e} + \sum_{e=1}^{M_s} \frac{\partial F_S^e}{\partial \phi_{yi}^e} + \sum_{e=1}^{M_s} \frac{\partial F_E^e}{\partial \phi_{yi}^e} = 0 \qquad \text{(A23)}$$

$$i = 1, 2, 3, ..., N_y$$

$$\frac{\partial F}{\partial \phi_{zi}} = \sum_{e=1}^{M_v} \frac{\partial F_V^e}{\partial \phi_{zi}^e} + \sum_{e=1}^{M_v} \frac{\partial F_I^e}{\partial \phi_{zi}^e} = 0 \qquad \text{(A24)}$$

$$i = 1, 2, 3, ..., N_z$$

leading to a matrix system for the solution of the node fields. In (A22), N_x denotes the total number of element edges parallel to the x-axis and similar definitions hold for N_y and N_z. Also, ϕ_{pi} $(p = x, y, z)$ are the fields labelled with global indices, and as before ϕ_{pi}^e $(p = x, y, z)$ are the fields associated with the eth volume or surface element. Both ϕ_{pi} and ϕ_{pi}^e refer to the field at the same edge and thus the eth term of the summations has non-zero value only if the global edge i belongs to the eth element. The system implied by (A22)–(A24) must, of course, be solved after imposing the boundary condition (7) which permits us to zero out those field components that belong to edges on metallic boundaries. This reduces substantially the number of unknowns in the system which can then be solved via direct inversion, LU decomposition, or iteration. However, since the system matrix is partly full and partly sparse as well as symmetric and banded (if the nodes are properly

numbered), it can be more efficiently solved by those algorithms which exploit these properties. Various partition techniques can also be employed to enhance the efficiency of the solution. Further, the matrix system is amenable to a conjugate gradient–fast Fourier transform solution, as discussed in the text.

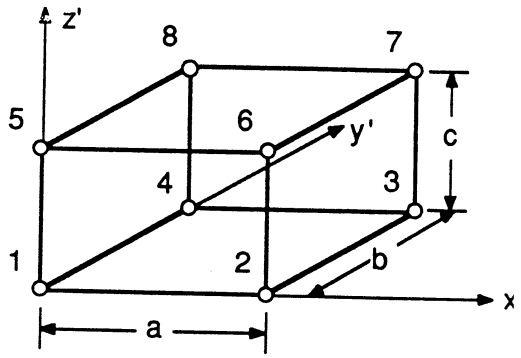

Figure A1: A rectangular brick.

APPENDIX 2

CAVITY3D MANUAL

CAVITY3D is a program which allows the user to study the radiation and scattering characteristics of a cavity in an infinite ground plane. The cavity may be filled with different dielectrics, while conducting patches, lumped loads, probe feeds and short circuit pins can be placed in it. Finally, the aperture may be covered by an R-card.

Since the program employs the FEM method, information pertinent to mesh generation, such as number of nodes, needs to be given. These inputs will, in effect, determine the computing time required, along with the accuracy of the results.

This manual will present an explanation for each input that the program requires.

INPUT 1 : INPUT DIMENSIONS OF THE CAVITY: XL,YL,ZL (in cm)

The first three numbers you will be asked to input will be the XL, YL, ZL. XL is the x-size, YL is the y-size, and ZL is the depth, of the cavity. All numbers are actual dimensions in cm.

INPUT 2 : INPUT NUMBER OF POINTS ALONG EACH CAVITY SIDES: NX,NY,NZ

The next step is to specify the number of nodes inside the cavity. Since NX and NY are the number of nodes, NX-1 and NY-1 will be the number of elements, in the x and y directions respectively. The program uses a Fast Fourier Transform (FFT) to solve the problem. The FFT pad size is related to NX and NY as follows:

NX ->	FFT pad x-size	NY ->	FFT pad y-size
2-7	16	2-7	16
8-15	32	8-15	32
16-31	64	16-31	64
32- 63	128	32-63	128

The size of the FFT pad is proportional to the computing time required, whereas more nodes will increase the accuracy of the results. If, therefore, you were to pick 16 for NX and NY instead of 15 you would be increasing the computing time tremendously (FFT pad=64x64 vs FFT pad=32x32) without a significant increase in accuracy. If on the other hand you had to choose a number above 15 for NX and NY the wise choice would be 31. Anything below 31 and above 15 would require the same computing time (FFT pad =64x64 for that range), but would decrease the accuracy (fewer nodes).

NZ is the number of nodes in the z-direction thus giving NZ-1 layers and elements in the same direction, with layer 1 being the topmost.

For the program to give accurate results, a good rule of thumb is to keep the element sizes smaller than a fifteenth of a guided wavelength.

Xelement size=XL/(NX-1) < $\lambda_g/15$

Yelement size=YL/(NX-1) < $\lambda_g/15$

Zelement size=ZL/(NX-1) < $\lambda_g/15$

Note: λ_g is the wavelength in the dielectric.

Example: A small mesh

XL=2cm NX=3 DX=XL / (NX-1)=1cm
XY=3cm NY=4 DY=YL / (NY-1)=1cm
XZ=1cm NZ=2 DZ=ZL / (NZ-1)=1cm

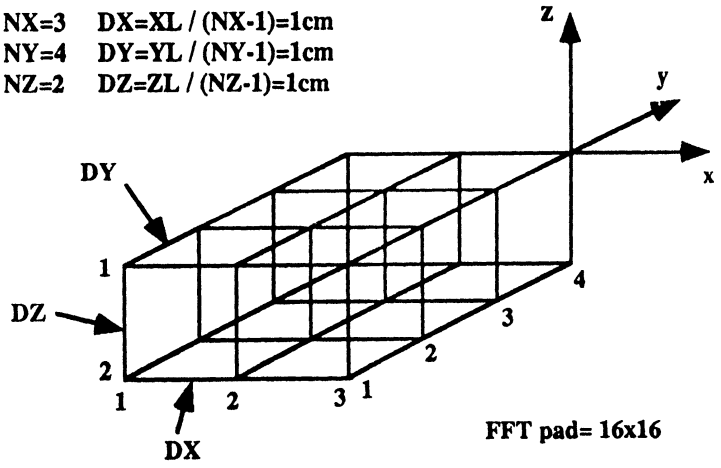

NOTE: Each cube is a cell. Each edge of a cube is an element and each corner is a node.

INPUT 3 : IS THE CAVITY FILLING HOMOGENEOUS? 1)YES 2)NO

If you answer 1 (i.e. YES) to the next prompt you will be asked to specify the relative permeability and permittivity. The whole cavity will then be filled with that dielectric.

If you answer 2 (i.e. NO) you will then need to input for each of the NZ -1 layers, the thickness in cm along with the relative permeability and permittivity, starting with layer 1 (ie the top layer). The program will prompt you for each successive layer separately.

Note that ε_r and μ_r are complex numbers. If, for example, ε_r =2-j1 and μ_r =1+j0 then the inputs would be (2.,-1.) and (1.,0.) respectively.

INPUT 4: INPUT BEGINNING, FINAL AND INCREMENTAL FREQUENCIES:

By specifying (in GHz) the initial, final and incremental frequencies you may perform a frequency sweep. If you desire to run the program at only one frequency, let's say 10 GHz, then your input should be: 10 10 1

INPUT 5: INPUT KODE: 0 FOR BISTATIC SCATTERING
1 FOR BACKSCATTERING
2 FOR RADIATION

A: 2=Radiation

If the choice is 2 then radiation characteristics such as radiated intensity and input impedance will be computed. The next two inputs will determine the point(s) in space, where the radiated intensity will be evaluated.

Input A1: FOR RADIATION PATTERN COMPUTATION,
INPUT BEGINNING, FINAL AND INCREMENTAL ANGLES:
PHIBEG,PHIFIN,PHISTP (in degrees)

ϕ is the angle as defined in the conventional spherical system(i.e. in the x-y plane and measured from the x-axis). Its initial, final and incremental values have to be given in degrees. For example, an input of 0 90 2 will perform the radiation computations for ϕ =0,2,4,6,8,10,12,.....,90 degrees. If the input is 90 90 1 then ϕ =90 degrees for all computations.

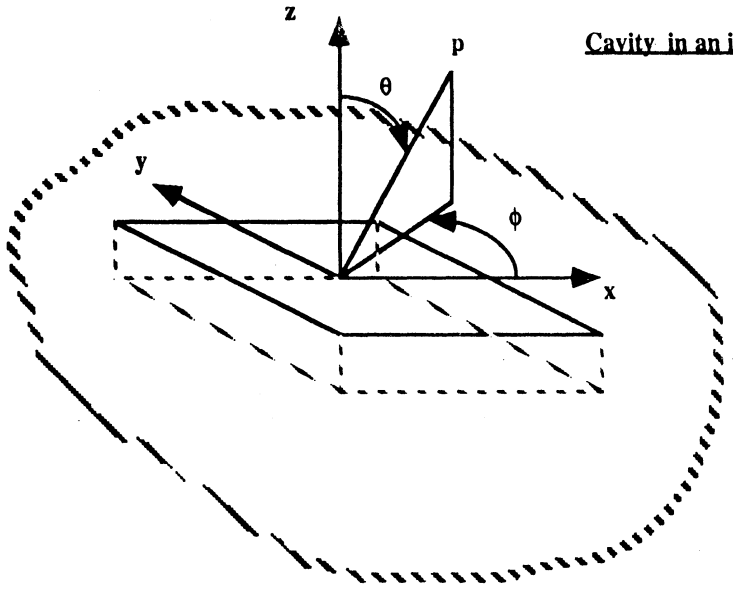

Cavity in an infinite ground plane.

Input A2: INPUT BEGINNING, FINAL AND INCREMENTAL ANGLES:
THEBEG,THEFIN,THESTP (in degrees)

θ is the angle as defined in the conventional spherical system(i.e. measured from the z-axis). Its initial, final and incremental values have to be given in degrees. For example, an input of 0 90 5 will perform the radiation computations for θ =0,5,10,15,20,25,30,.....,90 degrees. If the input is 0 0 1 then θ =0 degrees (i.e. normal incidence) for all computations.

Input A3: INPUT TOLERANCE AND MAXIMUM ITERATIONS: TOL(~.01),ITMAX

At this point the program will request the tolerance and maximum iterations. A tolerance of 0.01 is a good choice. Also choosing the number of maximum iterations to be 500-1000 is quite appropriate. If the max number of iterations is exceeded before the residual falls below the specified tolerance value then the program halts.

Input A4: MONITOR THE SOLUTION CONVERGENCE? 1)YES 2)NO

Sometimes the program converges long before it satisfies the tolerance requirement. To save time one can monitor the solution convergence by answering 1 (ie YES) to this prompt. The residual (RSS) is then displayed for each iteration during output. The RSS value is expected to "hop around". If the computed radiated intensity and input impedance values remain relatively constant for each iteration then convergence has been achieved.

```
FFT PAD SIZE: NXFT =              NYFT =
SURFACE ELEMENT SIZE:  DX=                    DY=
```

The program at this point will let you know what FFT pad size will be employed along with the surface element size, where: DX=XL/(NX-1) and DY=YL/(NX-1)

Input A5: NUMBER OF CONDUCTING PATCHES: NPATCH

The number of conducting patches that will be placed in the cavity is then requested. The patches are rectangular in shape. In order, therefore, to create a different geometry, a collection of patches must be used. For each patch, the user needs to specify the following.

```
INPUT FOR THE PATCH #          1
POSITION OF THE LEFT BOTTOM CORNER OF THE PATCH
IN TERMS OF NODES: NCX,NCY
```

1) The lower left corner of the patch in terms of cavity nodes NCX, NCY. (This positions the patch on the x-y node coordinate plane)

```
PATCH DIMENSION IN TERMS OF SEGMENTS: MX,MY
```

2) The number of elements along the x and y directions on the patch. This actually dimensions the patch, since the element sizes in the x and y directions have already been determined. Their values are the surface element sizes DX and DY.

```
ON WHICH INTERFACE DOES THE PATCH RESIDE: NSUR
NSUR = 1 IF THE PATCH SITS AT THE TOP OF THE 1ST LAYER
 2 IF THE PATCH SITS AT THE TOP OF THE 2ND LAYER
ETC.
```

3) The layer on which the patch sits on. You may pick from a total of NZ-1 layers.

Input A6: `PATCH GEOMETRY DISPLAY? 1)YES 2)NO`

If a patch display is chosen then a graph of the cavity and the patch is shown. The stars indicate conducting patch surface elements and the dots represent cavity (dielectric) surface elements. Each dot or star can be thought of as a surface rectangular element of dimensions DX, DY.

Input A7: `NUMBER OF SHORT-CIRCUIT PINS: NPIN`

Here you are required to specify the total number of short - circuit pins to be placed in the cavity. If you do not wish any, just input 0. For each pin its coordinates in terms of nodes will be requested.

Then the layer in which it is placed will be asked for.

Note that if you have more than one layers you will need to stack pins one under the other, all the way to the ground, in order to get a short.

```
TOTAL NUMBER OF UNKNOWNS =
```

At this point the program will output the total number of unknowns it will have to solve for. This should give you an idea of the size of the problem it will attempt to tackle.

Input A8: INPUT NUMBER OF PROBE FEEDS: NFEED

The total number of probe feeds is then requested. Note that without a feed all radiation characteristics will be zero.

INPUT LOCATION OF THE FEED # 1 : LFX, LFY

For each feed the first input required is its location in terms of nodes LFX, LFY.

INPUT AMPLITUDE AND PHASE OF THE PROBE CURRENT: CAM,CPH

Second you need to input the magnitude and phase of the current.

IN WHICH LAYER IS THE FEED EMBEDDED: NLAY

Finally you will have to give the layer in which the feed is embedded . This number will range between 1 and NZ-1.Note that if you need to have the feed running from the top to the bottom of the cavity and you have more than one layers you may need to stack NZ-1 (=total number of layers) feeds one on top of the other.

Input A9: INPUT NUMBER OF IMPEDANCE LOADS: NLOAD

Here you are asked to input the number of lumped loads you wish to place in the cavity. If you do not wish any, just type 0 and hit return.

INPUT LOCATION OF THE IMPEDANCE LOAD # 1 : LDX, LDY

For each load, first its coordinates in terms of nodes will be requested.

INPUT VALUE OF THE IMPEDANCE LOAD: ZL (COMPLEX)

Second its impedance, will have to be specified. If for example ZL=500 +j30 Ω then the input will be (500.,30.).

IN WHICH LAYER IS THE LOAD EMBEDDED: NLAY

Finally you need to input the layer in which the load is placed, which will be a number between 1 and NZ-1. Note that if you have more than one layers and you want your loads to start from the surface of the cavity and touch the ground at its bottom you will need to specify as many loads as the layers and stack them one on top of the other.This will add their impedances in series.

Input A10: CAVITY APERTURE COVERED BY A RESISTIVE CARD? 1)YES 2)NO

A choice regarding a resistive card covering the cavity is presented. An input of 2 (ie NO) will leave the cavity "as is", i.e. without an R-card. An input of 1 (ie YES) will cover the cavity with an R-card.

Then you will be prompted to specify the R-card resistivity (normalized to the free space intrinsic impedance 377Ω).

```
INPUT NORMALIZED RESISTIVITY: ETA (COMPLEX)
NOTE: IF ETA IS A FUNCTION OF POSITION,
      SPECIFY IT IN SUBROUTINE RESIS
```

If instead of a uniform resistivity a spatially varying one is needed you have to specify it internally, within the subroutine RESIS. In this subroutine a place is specified for such customization. If this is done, then the R-card value you input externally is disregarded. An example of such a customization and its effects on the R-card resistivity is attached.

```
      SUBROUTINE RESIS(AX,AY,EX,EY,NSX,NSY,NX,NY,NZ,DX,DY,KO,ETA)
C*********************************************************************
C.....THIS SUBROUTINE ADDS THE RESISTIVE SHEET'S CONTRIBUTION TO AX  *
C ... AND AY                                                         *
C*********************** ***********************************************
      COMPLEX AX(*),AY(*),EX(*),EY(*),ETA,CJ,A1,A2
      REAL KO
      INTEGER NSX(2,*),NSY(2,*)
      NX1=NX-1
      NY1=NY-1
      NXT=NX1*NY*NZ
      NYT=NX*NY1*NZ
      CJ=CMPLX(0.0,1.0)
      A1=CJ*KO*DX*DY/(3.*ETA)
      A2=0.5*A1
      DO 703 J=1,NY1
      Y=(FLOAT(J)-0.5)*DY
      DO 703 I=1,NX1
      X=(FLOAT(I)-0.5)*DX
C*********************************************************************
C.....IF ETA IS A FUNCTION OF X AND Y, SPECIFY HERE
C
c Note: If a variable resistivity is required it can be specified
c       internally at this point. The example below places a tapered
c       R-skirt 6 elements wide at the cavity edges. We assume that the
c       cavity has 61*61 nodes or 60*60 elements on its surface.
c       i denotes the x-node coordinate and j the y-node coordinate
c       The normalized resistivity is eta and is a complex number.
c       Its value starts from a value of 1 and ends at .1 . Note that
c       outside the R-skirt eta=(8000.,0.), which makes
c       the R-card in this region to be treated as free space.
c       Finally you need to be aware that very low resistivities
c       ie R<.1 might cause convergence problems.

      if ((i.ge.55).or.(j.ge.55).or.(i.lt.7).or.(j.lt.7)) then
      eta=(1.,0.0)
      else
      eta=(8000.,0.0)
      endif
      if ((i.ge.56).or.(j.ge.56).or.(i.lt.6).or.(j.lt.6)) then
      eta=(.8,0.0)
      endif
      if ((i.ge.57).or.(j.ge.57).or.(i.lt.5).or.(j.lt.5)) then
      eta=(.6,0.0)
      endif
      if ((i.ge.58).or.(j.ge.58).or.(i.lt.4).or.(j.lt.4)) then
      eta=(.4,0.0)
      endif
      if ((i.ge.59).or.(j.ge.59).or.(i.lt.3).or.(j.lt.3)) then
      eta=(.2,0.0)
      endif
      if ((i.ge.60).or.(j.ge.60).or.(i.lt.2).or.(j.lt.2)) then
      eta=(.1,0.0)
      endif

      A1=CJ*KO*DX*DY/(3.*ETA)
      A2=0.5*A1
C*********************************************************************
      K=(J-1)*NX1+I
```

B: 1=Backscattering

If you choose 1 then the backscattered power will be computed (ie transmitter and receiver are located at the same place).

Input B1: INPUT POLARIZATION ANGLE: ALPHA (in degrees)

Here you are asked to input the polarization angle α. If $\alpha=0$ then the incident wave is TM and if $\alpha=90$ it is TE.

The next two inputs determine the directions at which the receiver and the transmitter are placed.
A θ and ϕ have to be specified the same way they were for the radiation pattern computations. From here on all subsequent program inputs have already been described in the Radiation option (i.e. part A of this manual).

C. 0=Bistatic Scattering

If you choose 0 for the code then the transmitter and the receiver can be at different locations, that is you will have chosen the bistatic scattering option.

Input C1: INPUT INCIDENCE ANGLE: PHIINC,THEINC (in degrees)

For bistatic scattering, the first input required is the direction of the incident wave. This is achieved by specifying the θ and ϕ angles in degrees (as defined in the conventional spherical coordinate system). θ can range from 0 to 90 degrees and ϕ from 0 to 360 degrees.

The next step is to specify the polarization angle α . This input, along with all subsequent ones have been described in the Radiation case (i.e. part A of this manual).

```
      L1=NSX(1,K)
      L2=NSX(2,K)
      AX(L1)=AX(L1)+A1*EX(L1)+A2*EX(L2)
      AX(L2)=A X(L2)+A2*EX(L1)+A1*EX(L2)
      L1=NSY(1,K)
      L2=NSY(2,K)
      AY(L1)=AY(L1)+A1*EY(L1)+A2*EY(L2)
      AY(L2)=AY(L2)+A2*EY(L1)+A1*EY(L2)
703   CONTINUE
      RETURN
      END
```

Typical input file

```
7.5  5.1  .17558        cavity size in cm (x,y,z)
31  31  2               number of nodes (x,y,z)
1                       - uniform dielectric
(2.17,0)  (1.,0.)       substrate dielectric - εr  μr
1.97  1.97  1           frequency  min, max, increment
2                       - radiated intensity calculation
0  0  1                 theta  min, max, increment
0  0  1                 phi    min, max, increment
.01   800               tolerance, number of iterations
2                        - monitor cnvergence 1=yes 2=no
1                       number of patch
6  6                    lower left corner of patch node(x,y)
20  20                  number of elements on patch (x,y)
1                       layer in which patch resides
2                        - patch display 1=yes 2=no
0                       number of short circuit pins
1                       number of feeds
11  11                  feed position node(x,y)
1  0                    amplitude and phase of current source
1                       layer in which feed is embedded
4                       number of loads
15  6                   node(x,y) load 1 position
(300.,0.)               value of load 1 (complex) in Ω
1                       layer in which load 1 is embedded
25  15                  node(x,y) load 2 position
(300.,0.)               value of load 2 (complex) in Ω
1                       layer in which load 2 is embedded
15  25                  node(x,y) load 3 position
(300.,0.)               value of load 3 (complex) in Ω
1                       layer in which load 3 is embedded
6  15                   node(x,y) load 4 position
(300.,0.)               value of load 4 (complex) in Ω
1                       layer in which load 4 is embedded
2                       - resistive card 1=yes 2=no
```

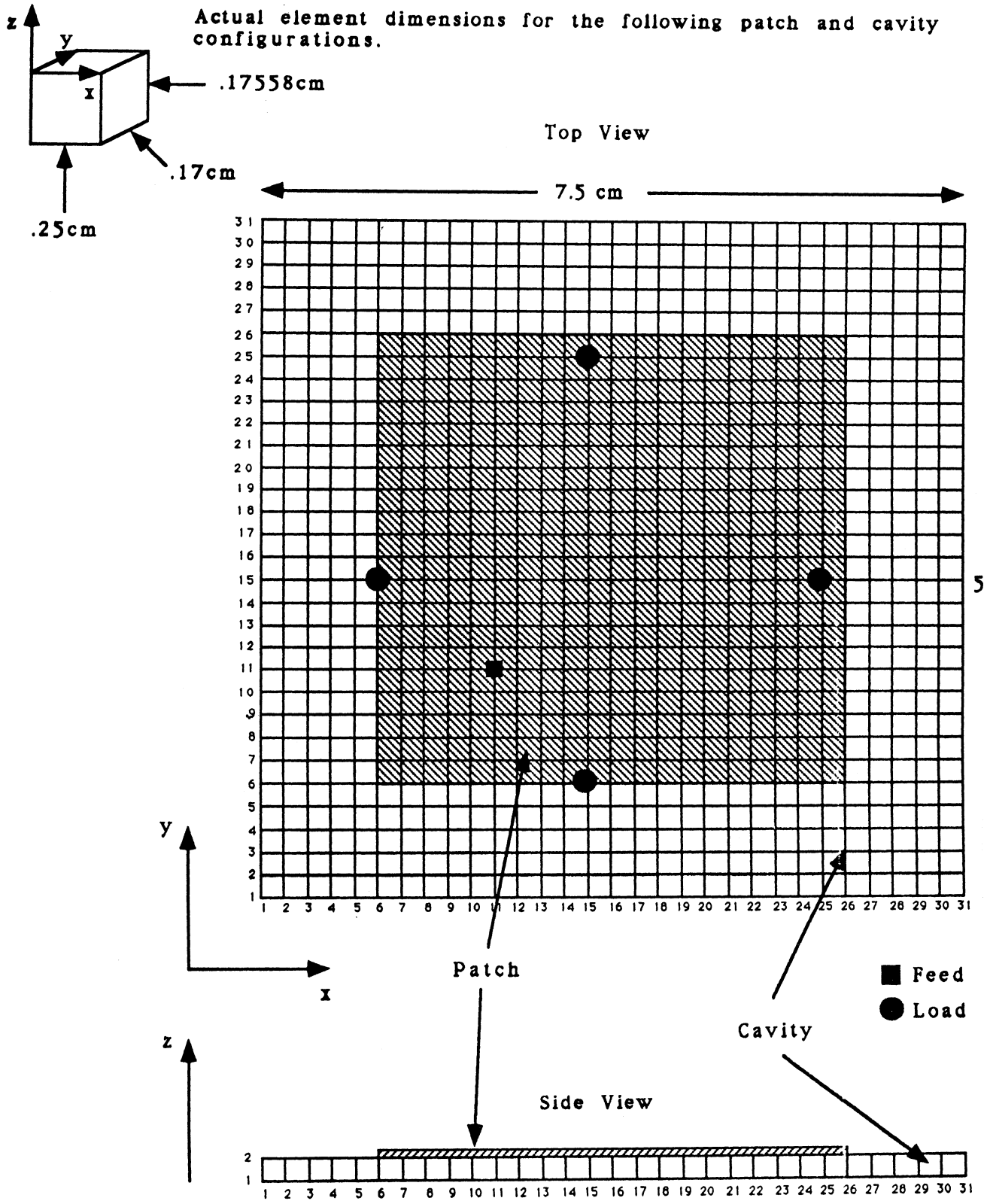

Patch dimensions : x-5.0cm, y-3.4cm

This is the exact patch-cavity configuration resulting from the input file given.